Evaluation of C/C-SiC Composites for Small Motor Components

Randy Lee . . . . . June 2008

Marshall Space Flight Center

Introduction

The following discussion is a compilation of notes and comments generated during the period Feb '08 to June '08 regarding issues associated with the Carbon/Carbon-Silicon Carbide (C/C-SiC) composite articles used in the Attitude Control Motor (ACM) of the Launch Abort System (LAS) for the Orion Crew Exploration Vehicle (CEV). The motor/valves for the ACM are currently been designed, developed and assembled by ATK who is sub to Lockheed with Orbital as an intermediary and XYZ as the actual manufacturer of the C/C-SiC components. The motor is intended to fire for several seconds while the internal valve section is expected to see flame temperatures of 3200°F and pressures close to 2000 psi during the burn cycle. In addition to other components within the valve cavity, certain regions and surfaces of the C/C-SiC components are expected to see conditions close to these in a very short period of time. The intent behind FMI's design and construction of the C/C-SiC material is to provide a substantial level of improvement in mechanical and thermal shock protection when compared to some of the other non-metallic material candidates available, particularly those based on more common C/SiC composites. This overview is concerned with the materials, manufacturing processes, properties and possible failure mechanisms associated with the C/C-SiC articles for the more recent HT-7 motor test valve. It is intended strictly to address the C/C-SiC composite material – not the design, analysis or operation of the motor/valve. In addition, these notes are based solely on information made available to the author to date and no guarantee is given regarding any inaccuracies or implications related to other unseen data.

Background

The pintle and guide components in the valve section of these motors are machined articles taken from larger C/C-SiC densified slabs which are produced via 3-D carbon composite fabrication, ceramic matrix densification and ceramic coating. Initially, XYZ fabricates a specially woven 3-dimensional bulk fibrous billet which contains carbon fiber bundles running along 4 unique directions. The *u*, *v* and *w* fiber orientations each form a layer in parallel planes somewhat analogous to the unidirectional *x-y* laminate plane while the *z* fiber direction runs perpendicular through the *u-v-w* lamina structure. However, other than point-to-point contacts at bundle intersections, none of the bundles are interlaced, interlocked, interconnected or crimped in any way and thus, each of the *u*, *v*, *w* layers simply consist of parallel bundles in the same plane. with no weave interactions With fiber bundles around 15 mil in diameter, each repeating *u, v, w* sequence probably runs about 40-50 mil in thickness while z bundle spacing is on the order of 0.05". Representative illustrations for the three directions of interest in the preform architecture have been produced and given in Figure 1[1].

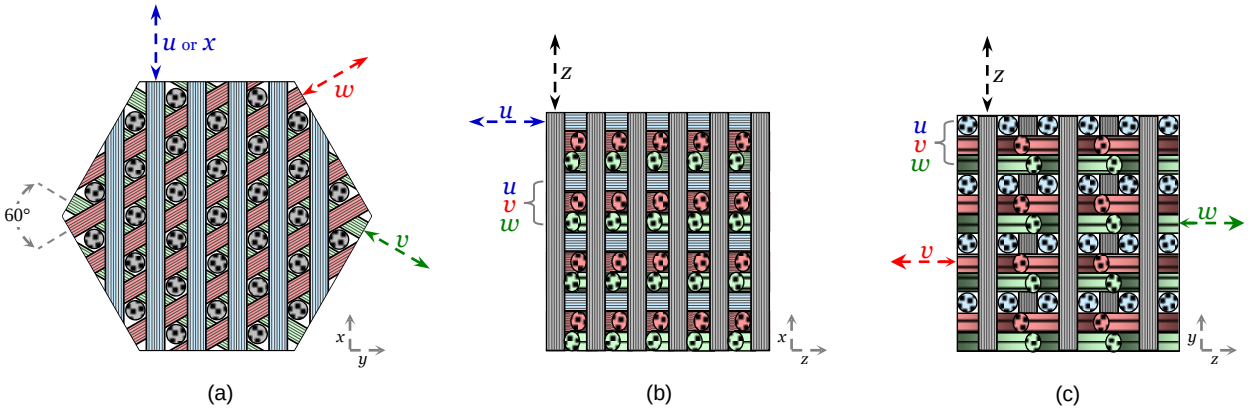

Figure 1. Cross-sectional views of the 4-directional preform weave architecture utilized by XYZ for the HT-7 components[1] . . . (a) Perspective looking down the *z* axis onto the *x*-*y* plane; (b) Perspective looking along the *u* + 90 direction (the *y* direction) onto the *x*-*z* plane (recall there are no bundles parallel to *y;* *u* bundles are perpendicular); (c) Perspective looking down the *u* direction (the arbitrary *x* axis) onto the *y*-*z* plane (*v* bundles come in from the right, *w* bundles come in from the left at 120° apart).

For reference, the *x* axis can correspond to any of the *u*, *v*, *w* directions but has no principle orthogonal counterpart on the same plane since the three fiber directions are sequentially oriented 60° relative to one another (*x* can be assigned to the *u* axis for beginning discussions). This pseudo-quasi-isotropic configuration allows one to assume that properties along any of the principle *u*, *v* and *w* directions are equivalent, while the designation "*u*+90" refers to a direction (in the same *x*-*y* plane) that is orthogonal to any of the *u*, *v*, *w* orientations. Likewise, all of the *u*+90 directions can also be considered equivalent to each other, that is, *u*+90 = *v*+90 = *w*+90 (*u*+90 might be visualized as the *y* counterpart to *x*). Hence, there are no fibers directly oriented in the *u*+90 direction since it is comprised of contributions from two corresponding bundles at 60° to each other. Since there are no 3-D radial are pyramidal fiber bundles relative to the *z* axis or the *u*-*v*-*w* plane, this design is just an off-shoot to standard 3-D orthogonal architectures. Also, to avoid confusion, the "D" in XYZ's "4-D" nomenclature refers to "directional" while in traditional preform classifications, "3-D" is standard nomenclature for generalized 3-Dimensional preform architectures in which all multi-directional "n-D" weaves fall under.

The fibrous material used to construct the preform billets for the more recent valve articles was derived from high modulus carbonized PAN fibers manufactured by Grafil (a subsidiary of Mitsubishi) and is designated as Pyrolfil HS40. 'High modulus' usually implies that the fiber bundles are subjected to higher carbonization temperatures and tensioning effects during their manufacture. These processing conditions tend to increase longitudinal orientation of fiber microstructures leading to more pronounced alignment of the 2-D graphene basal layers (sheets of fused polynuclear hexagonal carbon rings) which leads to . . . higher thermal conductivity along the fiber length. HS40 is given as the highest conductivity fiber in the entire Grafil/Pyrofil product line[2] at 52 W/mK (lateral or transverse thermal conductivity is substantially lower due to basal layer misalignment). The individual fibers are a small 5μ in diameter which allows Grafil to form high tow yarns in large 12K bundles. The bundle tensile strength for the raw material is given as 670 ksi per bundle which is in the upper echelon of the Grafil/Pyrofil carbon fiber product line. The unique PAN precursor material used to form the HS40 fiber is supplied directly from Mitsubishi Rayon which produces their own PAN filaments in-house. High modulus PAN fibers are known to have a longitudinal CTE of about -0.5 to 0.5 (X 10^{-6}/°C) over a very wide temperature range while the transverse CTE has been reported to be 4 and above[3]. This means that thermal expansion across the diameter of the fiber (transversely) is at least 4 times greater than that along its length (i.e... the fibers get fatter while their lengths remain about the same). Longitudinal alignment established during processing imparts sort of an orthotropic character to the fiber but the interlayer 'd' spacings between graphene sheets are still quite loose and subject to thermal mobility. It goes without saying, composites fabricated from these fibers will take on a substantial degree of the properties and behavior imparted by the fibers themselves.

[1] Data and information taken from the presentation, "XYZ Ceramic Matrix Composite System" for the Orion LAS ACM. Information, illustrations and formats may be simplified, enhanced or reduced to fit the objectives of this discussion without loss in accuracy or correctness.

[2] Information taken from the product data sheet for Pyrofil™ HS40 (www.grafil.com)

[3] Information acquired from independent, multiple or undisclosed sources.

The HS40 fiber density is given as 1.85 g/cm^3 which probably reflects its true or real density as measured via x-ray diffraction. Note that this density is substantially lower than that of pure 3-D graphite (x-ray density 2.26 g/cm^3). This is partially due to crosslinks established during the stabilization treatment in the fiber manufacturing process and because fusion between cyclic acrylonitrile rings is so massive that the carbonized structure is essentially 'thermoset' in space without much mobility to undergo true graphitization. As such, carbonized PAN (and rayon) fibers are generally classified as 'hard' carbons which exhibit minimal crystallization, even after relatively high exposure temperatures. While there may be a few regions or domains here and there containing graphitic-like structures, for the most part, these fibers are essentially 'amorphous' throughout where the basal sheets (or ribbons) tend to orient longitudinally along the fiber length but are spaced apart in a turbostratic-like manner in the transverse direction. Truly graphitizable carbon fibers can be obtained from mesophase coal tar and petroleum pitch materials (and pyrolytic graphite fibers formed via CVD) under special conditions.

Initially, the freshly woven dry preform billet used to form the HT-7 articles contained about 55-60% open void space overall[1]. The total void volume is a combination of the space between all the fiber bundles within the weave structure (inter-tow porosity) and the voids and porosity in between the all the fibers within each of the bundles (intra-tow porosity). It is also known that even the individual fibers or filaments themselves are porous. However, not all of this porosity is 'open' – much of the fiber porosity is closed-off and inaccessible to impregnating fluids or CVI gases. This is also true of some of the intra-bundle porosity. A substantial fraction of the 'total' porosity occurs at many of the *u*, *v*, *w*, and *z* bundle intersections which ultimately take the form of closed-off cavities at some point during the densification process (to be discussed later). Thus, the given 55-60% void volume refers to total fraction of voids, cavities and porosity within the dry preform structure which may or may not be accessible to intruding densification resin (some of this volume will inevitably become sealed off during the matrix densification process). Since the bulk volume of the billet (or slab) changes very little, if any, throughout the manufacturing process, the fiber volume fraction for the composite remains approximately constant at 40-45% throughout the entire process. Also, due to obvious directional differences in bundle spacing (or bundle density along the various planes, effective fiber volume fractions for each of the *u*, *u*+90 and *z* domains are expected to differ.

Now dry fibrous preform structures are usually limp and will tend to distort, warp and lose their shape when handled unless the fabricator 'rigidizes' the open preform structure by applying a thin coating to the internal fiber surfaces. This is typically accomplished with either a short gaseous CVI step, which deposits a thin but hard layer of pyrolytic carbon or polycrystalline SiC onto the fiber surfaces, or possibly by a very gentle liquid impregnation process using a thermoset polymer or an inorganic (silicate) sol-gel dispersion which is then subjected to curing and/or pyrolysis. The exact method used by XYZ to rigidize these preform billets prior to densification processing is unknown at this time. A short polymer impregnation step might utilize one of the more common crosslinkable linear polymers, perhaps something like styrene or acrylic-crosslinked polyester or even a silicone resin. Subsequent pyrolysis of a preform rigidized in this manner will consume much of the low char polymer but will leave enough carbon (and/or carbosilane) deposit to yield a stiffened preform structure that can be handled, moved around and is ideal for the subsequent pitch and ceramic matrix densification processes.

The fully densified billet or slab is designated as a "C/C-SiC" composite (rather than just C/SiC) because the very first densification cycle applied to the porous, rigidized preform utilizes a single impregnation with carbonaceous pitch followed by a 3000°F pyrolysis (carbonization) step. Figure 2 gives an abbreviated version of the process flow for the C/C-SiC billet/slab as provided by provided XYZ[2], but showing only particular steps relevant to the current discussion (labeled process temperatures were acquired from an independent source).

[1] Value taken from the presentation, "XYZ Ceramic Matrix Composite System" for the Orion LAS ACM.

[2] Data and information taken from the presentation, "XYZ Ceramic Matrix Composite System" for the Orion LAS ACM. Information, illustrations and formats may be simplified, enhanced or reduced to fit the objectives of this discussion without loss in accuracy or correctness.

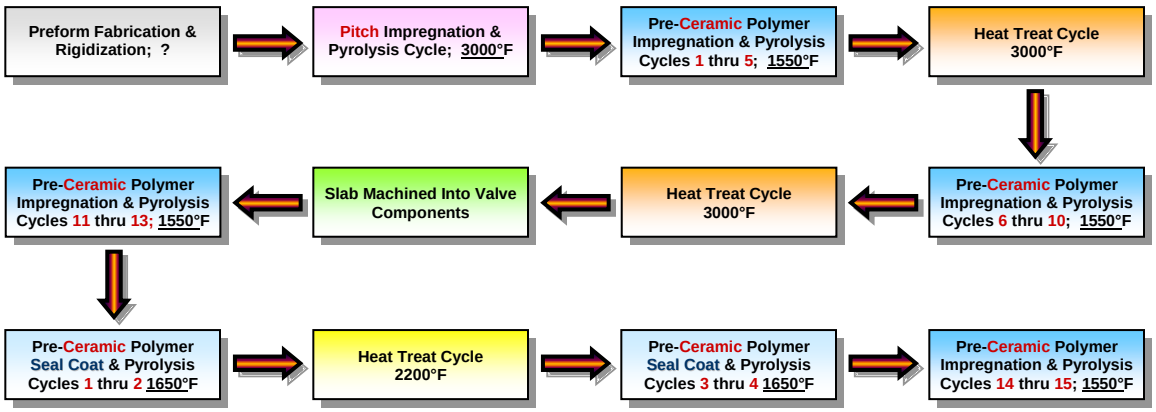

Figure 2. Abbreviated XYZ process flow for manufacturing of C/C-SiC slabs illustrating specific process steps from the preform state to the final coated form.

In general, each densification cycle consists of liquid impregnation into the porous, rigidized slab (under forces of vacuum, pressure, temperature or a combination of these) followed by pyrolysis. This process is often designated as Polymer Impregnation & Pyrolysis (or PIP). When the pitch densification cycle is complete, the slab (or substrate) is subjected to 13 densification cycles using a semi-inorganic, pre-ceramic polymer resinous material produced by Starfire Systems, SMP-10 (or AHPCS under the old nomenclature) which transforms into ceramic SiC upon subsequent pyrolysis. A final seal coat phase process is applied with this same material (or a modified version) using brush-on techniques and a couple of additional PIP cycles. Intermediate heat treatment steps are applied after several PIP cycles across the process sequence in efforts to advance ceramic conversion of the SiC matrix and to open up sealed voids and porosity within the substrate. Overwhelmingly, most of the internal and peripheral matrix in this composite is composed of SiC ceramic while the initial carbonized pitch deposit is like a thick fiber coating which acts, at least in part, as a bonding phase between the HS40 PAN fibrous reinforcement and the SiC matrix (in all practicality however, this is just a modified Ceramic Matrix Composite, CMC).

No specific chemical data is readily available for the particular pitch material used by XYZ for the carbon densification process. Independent sources have indicated that this was former AlliedSignal's 15V coal tar pitch whose future supply may be limited. It is well known however, that coal tar pitch materials used as binders are semi-solid hydrocarbon mixtures formed from the partial evaporation or distillation of coal tar. Industrial grade binder pitches are composed almost entirely of large polycyclic aromatic hydrocarbons (PAH) but also contain smaller aromatics such as anthracene, chrysene and benzopyrene along with a few aliphatic side groups and heterocyclic structures (non-aromatic, non-hexagonal aliphatics). Coking values (carbon yield) can run anywhere from 50 to 80% and most pitch mixtures do not have a distinct melting point but will soften and flow somewhere in the range 200°-350°F depending on the degree of polymerization and possible crosslinks, if any.

Coal tar pitches easily pass into mesophase and will readily graphitize when subjected to temperatures above 4000°-4500°F (all graphitizable carbon forms are classified as 'soft' carbons which must pass into mesophase in order to form the pre-graphitic 2-D structures necessary for transformation into 3-D graphite). As these pitch materials are heated beyond their melting ranges, the smaller molecules are either incorporated into the growing polyaromatic structure or they decompose and volatilize away. In the 600°-700°F regime, the material begins to undergo pyrolytic degradation in which PAH macromolecules coalesce, and hydrogen, methane and any latent oxygen begin to expel from the system. At around 750°-850°F, the pitch material enters a state of liquid crystal mesophase which is driven by advanced polymerization and the formation of discotic liquid mesophase particles or domains that continue to coalesce and grow as the temperature increases. In this state, the pre-graphitic microstructure of the transforming pitch material is comprised of layers of sp^2 bonded hexagonal carbon rings exhibiting long range 2-D order but with insignificant 3-D orientation. See Figure 3.

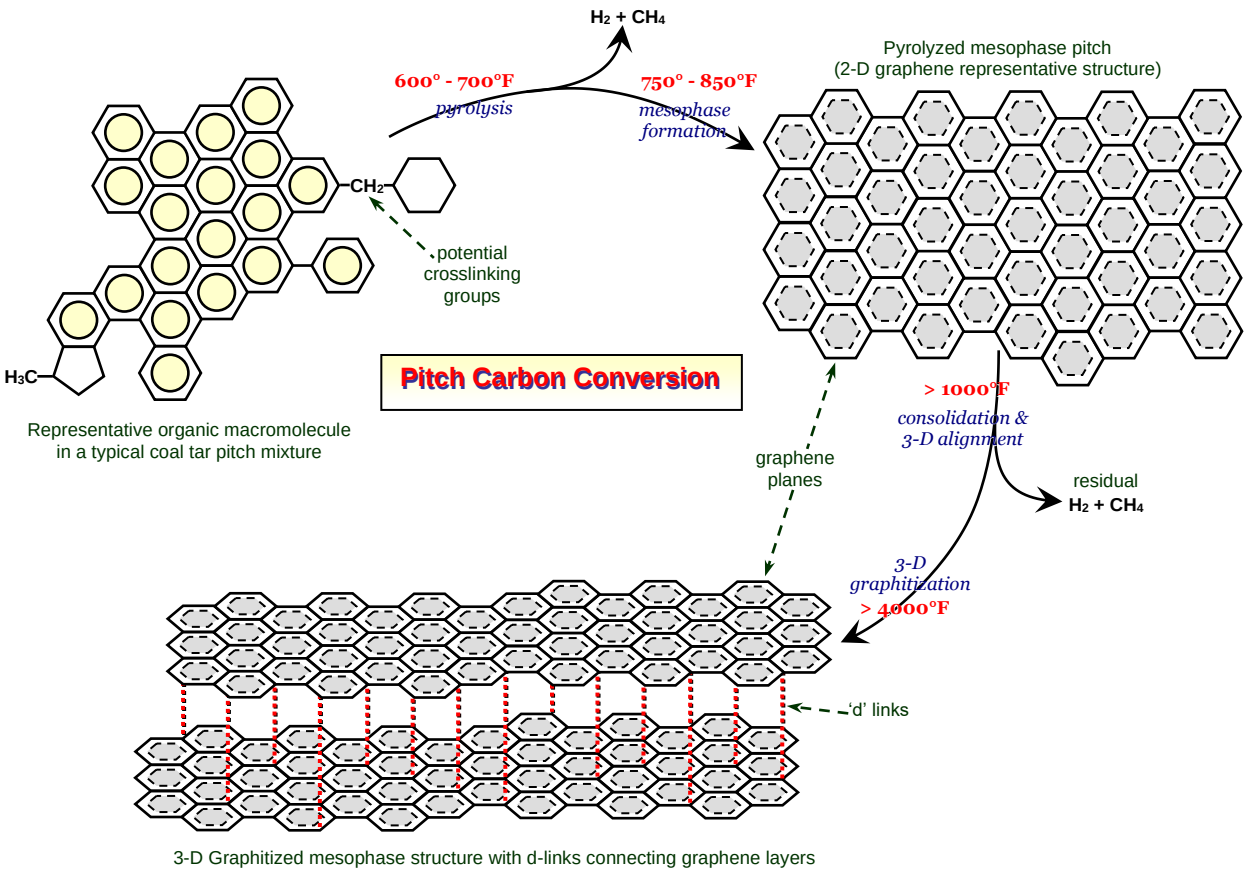

Figure 3. Likely pathway illustrating the thermal progress of carbonaceous pitch molecules as they undergo polymerization into 2-D graphene sheets, pyrolytic rearrangement, pass through mesophase and eventually transform into crystalline hexagonal close-packed graphite.

[1] Now these molecules are not linear polymers but are 'sheets' or layers comprised of aromatic (benzene) rings joined together in 2-D ribbon-like macrostructures which are highly anisotropic. As the reactions progress, mesophase (liquid crystal) particles continue to coalesce, getting larger and higher in molecular weight until around 950°-1000°F when the mesophase tar finally 'cures' into a non-melting solid carbon which can be classified as a 'green coke'. The macrostructure contains features of a material that has gone through a state of plastic flow and has solidified into an amorphous, highly anisotropic solid. Its (pre-graphitic) microstructure on the other hand, is composed of highly organized 2-D hexagonal graphene sheets with long range order in the 'a' crystallographic directions, but very little orientation the 'd' direction. This is due to the lack of indexing between graphene layers which can never be fully established until the material undergoes graphitization at temperatures above 4000°F. The actual value of these 'd-spacings' is determined by the nature of binding between indexed carbon planes in the ABAB graphite structure which is believed to be associated either with van der Waals interactions between carbon atoms in adjacent layers or by actual molecular overlap of their respective π orbitals. At any state prior to 3-D graphitization, the material is often classified as an 'amorphous' carbon. (The term 'amorphous' is used with the understanding that these types of carbon forms actually consist of 2-D graphene hexagonal layers with no distinct 'd' alignment or indexing – they are disorganized structures in a 3-D sense but are hexagonal at the 2-D level as illustrated in Figure 3.).

[1] All chemical structures, reactions, mechanisms and descriptions are solely the perception of the author and no guarantee is made regarding their accuracy.

Other than the 3000° heat treatment / pyrolysis cycle indicated in the process flow after the pitch impregnation step (Figure 2), parameters for the pitch densification step utilized by XYZ are unknown at this time. Most likely, the heated pitch is drawn into an impregnation chamber (containing the billet) under vacuum forces followed by pressure application to facilitate intrusion of the hot liquid pitch into the billet porosity. They could have employed hot isostatic pressure (HIP) during carbonization for yield enhancement. Since >4000°F is necessary to convert any form of 2-D amorphous carbon into 3-D crystalline graphite, the 3000° heat treatment step indicated in Figure 2 is a strong indication of XYZ's intention to leave this portion of the composite matrix in a hardened mesophase, pre-graphitic (amorphous) state for these particular C/C-SiC billets. In a previous version of this material (based on G30-500 fiber), XYZ carried the heat treatment temperature for the pitch step all the way to 4600°, presumably with the intent to completely graphitize the pitch matrix fraction.

Now crystalline matrices are beneficial in load-bearing structural composites (in fiber-dominated systems) while amorphous matrix configurations will tend to dampen incoming mechanical and thermal shock waves thus protecting the reinforcement (in matrix-dominated composites). This applies to both carbon and ceramic matrices throughout. It is related to the mechanism in which the loads (or shocks) are transferred to the reinforcement and the end results desired. The effects of thermal shock are often associated with the production of microcracks which may eventually propagate and lead to fracture and failure. For applications requiring increased thermal conductivity and structural loading support from the fibers, crystallized matrices (such as graphite and β-SiC) might be incorporated into the composite matrix. However, crystalline matrices may also tend to reduce the composite's thermal shock resistance. For increased thermal shock protection (or lower thermal conductivity), amorphous matrix phases are often developed, as XYZ seems to have done with the current HS40-based material.

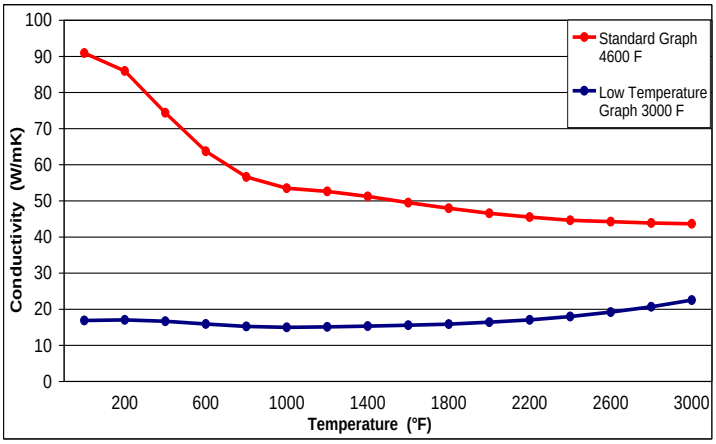

Figure 4. Thermal conductivity curve taken from the presentation, "XYZ Ceramic Matrix Composite System" comparing C/C-SiC material samples processed with pitch carbonized to 4600° to the current configuration utilizing 3000° carbonization.

These effects are illustrated in one of the charts provided by XYZ depicting the former G30-500 configuration (Standard Graph 4600F) in which the pitch matrix was graphitized, along with the current HS40 material (Low Temperature Graph 3000F) where the pitch matrix is left in the hardened mesophase (amorphous) state – see Figure 4. It is known that the thermal conductivity of 3-D graphite decreases over temperature (as indicated also in Figure 4), while that of amorphous carbons change very little until finally some of the 2-D graphene planes begin to line up at the higher temps. During the heating process, carbon-carbon bond lengths increase, and considering the highly anisotropic structure of graphite, this means heat transfer across the crystal lattice is slightly attenuated. On the other hand, the changing bond lengths tend to 'balanced out' in the amorphous (pseudo-isotropic) carbon until inter-layer associations (d-links) begin to form at the higher temps. Heat conduction through these structures is a combination of phonon propagation and π electron transfer. While phonon wavelengths are expanded in the hot crystal, they are non-existent in the amorphous structure, and collisions between π electrons in both structures increases with temperature. Overall, composite thermal conductivity is critically dependent on the thermal conductivities of the fiber and the matrix, the fiber volume fraction, the interfacial thermal resistance, and the porosity distribution in the composite.

Bonding between fibers and matrices in composites is usually a combination of mechanical interlocking and chemical associations or coupling. Since carbonized PAN fibers are highly porous, mechanical interlocking is significant. Chemical interactions between the carbonized pitch matrix and HS40 fiber surfaces may be a result of direct chemical bonding of fiber surface functional groups and carbonized pitch atoms along with extensive van der Waals forces and possibly π cloud interactions between matrix and fiber aromatic rings as matrix graphene sheets drape across the fiber surfaces. Partial oxidation of PAN fibers during processing along with other surface treatments are responsible for enhanced fiber-matrix interactions in composites throughout the industry. These treatments are designed primarily to accommodate organic matrices which can associate with functional groups formed on the fiber surfaces during such processing (oxygen-bearing matrix polymers such as epoxies, vinyl esters, phenolics, etc...). Typical functional groups generated on carbon fiber surfaces include hydroxyl, acyl and carboxyl groups which can interact with resin groups via hydrogen bonding, dipole interactions or direct coupling forming chemical links with ether or ester formation. Acidic carboxyl groups are predominant on carbonized PAN fibers. While these groups may readily interact with organic matrices at lower temperatures, the bonds will start to break down at higher temps. On the other hand, high napthalene/aromatic pitch carbons will tend to repel these interactions (sort of like trying to mix oil and water) until higher temperatures dissociate the carboxyl groups into free radicals which then bond directly with carbon atoms in the matrix. Thus far, there are no indications suggesting abnormally poor adhesion between the carbon matrix and fibrous phase in the HT-7 composite articles.

After the pitch PIP step is complete, the substrate (or rather the matrix) is densified through a series of ceramic PIP cycles using Starfire's SMP-10 pre-ceramic resin to form the SiC matrix phase within the composite's porosity . Compared to many densification resins, SMP-10 is low in viscosity (close to that of water) and has a low surface tension (that is, it wets the fibers well) making it a good intrusion fluid for substrate densification. Thirteen PIP cycles are indicated in Figure 2 as well as an additional two cycles applied during the coating phase (presumably to augment the seal coating process). The SMP-10 is a polycarbosilane material consisting of alternating carbon and silicon atoms along the polymer backbones in a highly branched structure with 10-15% allyl pendant side groups incorporated on strategic carbon atoms along polymer end regions to facilitate crosslinking (hardening) of the material prior to pyrolysis[1]. Initial PIP pyrolysis at 1550° transforms the cured polymer into glassy SiC[2] which is then converted into nano-crystalline β-SiC upon subsequent heat treatment to 3000° – all in the solid state. See Figure 4 [3]. An overall yield of 75-80% and a silicon-to-carbon ratio very close to 1:1 is typical.

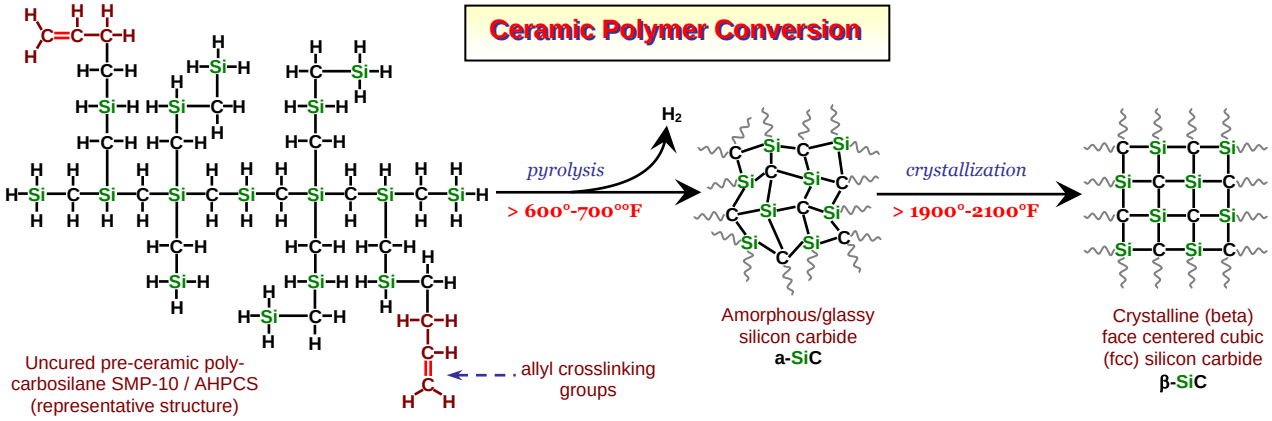

Figure 4. Likely structure of SMP-10 oligomer showing thermal progress as the material is transformed into a glassy ceramic at moderate pyrolysis temperatures and then undergoes crystalline transition at the higher temps.

[1] Information obtained via direct hands-on experience in the processing and characterization of these particular pre-ceramic resins combined with numerous consultations over the years with co-developer of the SMP-10 (AHPCS) product line in the 1990's, Dr. Walt Sherwood of Starfire Systems, New York.

[2] In this paper, the terms 'amorphous', 'glassy' and 'vitreous' may be used interchangeably to represent the same non-crystalline, glass-like state for a given material.

[3] All chemical structures, reactions and descriptions in this paper are solely the perception of the author; no guarantee is made regarding their accuracy or validity.

In its neat form, SMP-10 is a liquid resin which is often mixed with fine particles/powders to make a slurry that is forced into the porous substrate under vacuum (or brushed on during seal coating) and then cured to the 350°-500°F range under slight N_2 or Ar pressure if possible. The primary curing mechanism in the SMP-10/AHPCS system involves a typical free radical reaction scenario between allyl groups located at various branch end regions of each SMP-10 molecule which results in a highly crosslinked thermoset pre-ceramic product. Homolysis of polymer branches during cure generates radical fragments **R•** which initiate the process. See Figure 5.

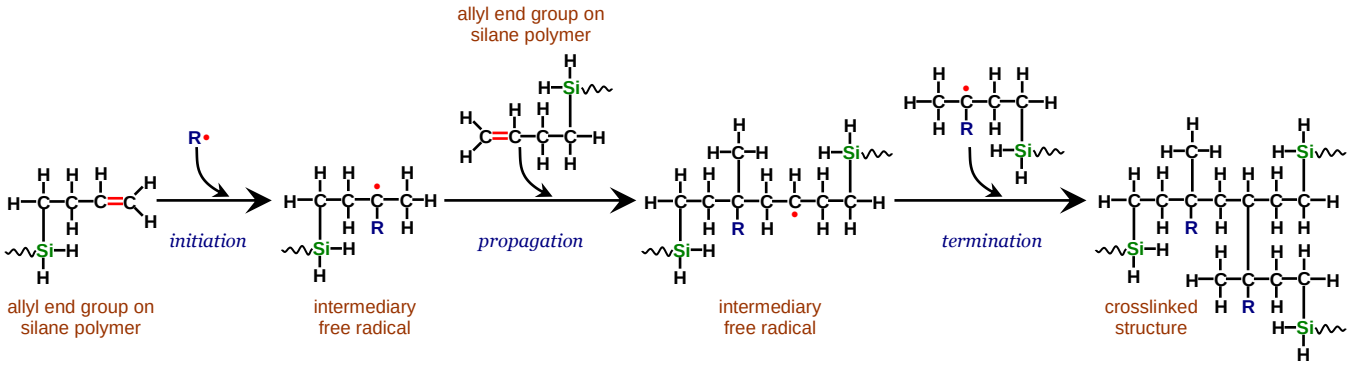

Figure 5. Sequence of likely reactions and molecular development as allyl groups in the curing SMP-10 polymer undergo free radical crosslinking with double bonds in neighboring molecules (or with allyl groups in the same molecule).

Early in the synthesis development of SMP-10, Starfire workers encountered difficulty attempting to incorporate simple vinyl groups into the polymer for crosslink capability but finally were able to attach the more reactive allyl (propenyl) group onto selected polymer end branches which resulted in acceptable crosslinks and curing properties. (The allyl radical is highly stabilized because the resonance structure is converted from an sp^3 hybridized carbon bond configuration to sp^2 and the π electrons are delocalized across the molecule . . . all of which permits easier interaction with carbosilane -CH_2-SiH_2- end groups.) However, a consequence of incorporating either one of these crosslinking monomers into the carbosilane polymer is a slightly higher level of carbon in the converted ceramic product. Also, one of the problems associated with these resins is their affinity to react with water and oxygen to form inter-molecular crosslinks and intra-molecular couplings. Traces of water or oxygen incorporated into the uncured resin mass due to atmospheric exposure or inadvertent processing conditions will cause siloxane links to form which may alter the ultimate ceramic stoichiometry and/or retard SiC formation leading to poor efficiency in the ceramic conversion process. See Figure 6.

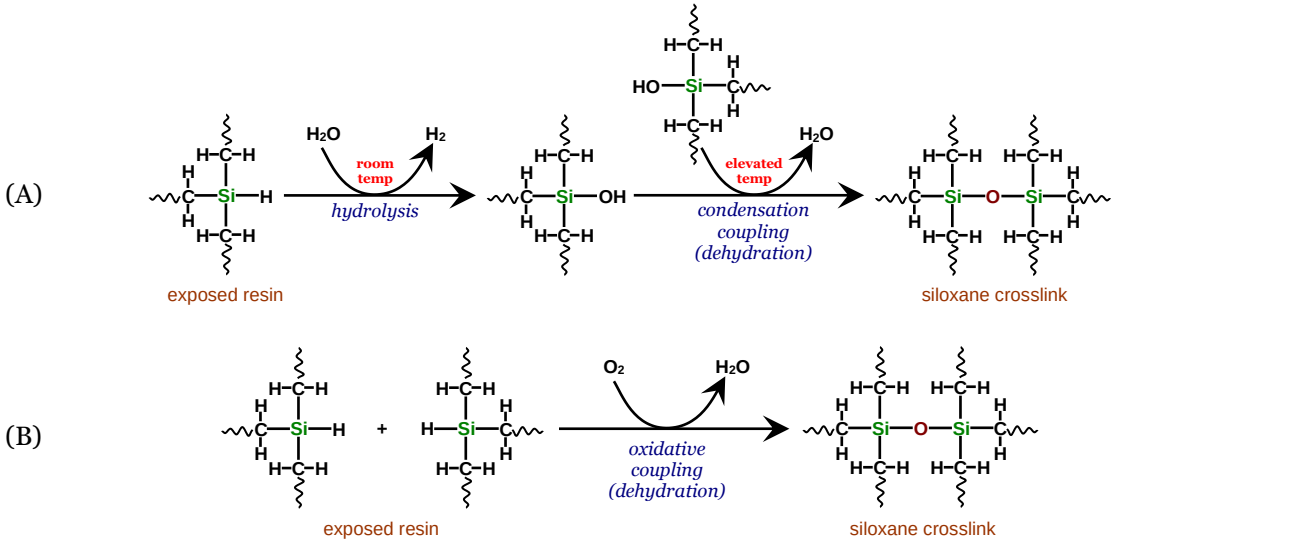

Figure 6. Likely side-reactions within the SMP-10 system affecting ceramic conversion properties. (A) Siloxane links formed by exposure to moisture; (B) Siloxane links formed by reaction with oxygen. In both cases, dehydration forms the coupling link.

As a result of the active hydrogens (hydride groups) attached to the silicon atoms, reactions (A) and (B) can occur during room temperature storage and all the way up the heating ramp as the polymer is cured and beyond. As low as room temperature, siloxane links and Si-Si bonds begin to form via hydrolysis and hydrogen abstraction respectively. At around 600°-700°F, the solid material begins to undergo pyrolysis which is accompanied by the release of hydrogen along with trace amounts of methane (due to degradation of organic groups) and trace levels of pyrophoric silanes. Siloxane groups begin dehydrating around 600°-650°F while Si-Si links rearrange at higher temperatures. A small fraction of these siloxane groups (as well as residual hydrogen) are still present after 700°-800° but are essentially all gone after the 1500°1600° pyrolysis cycle. In the 900°-1000° range, it is believed that the transition state di- and tri-silyl methyl radicals form and become the primary propagating species throughout the conversion of carbosilane polymer thermosets into 'green' ceramic SiC. Thus, the sequence of reactions comprising pyrolytic transformation of the SMP-10 polymer is believed to be a free radical driven process[1]. Pyrolysis converts the semi-organic (pre-ceramic) polymer into glassy/amorphous a-SiC (a non-oxide glassy ceramic). Ceramic yield from the liquid polymer state to 1600° is about 70-75%. This can be increased to ~80% if pressure is used. Glassy conversion results in bulk volume loss, structural consolidation and substantial porosity creation. This highly porous form is very susceptible to oxidation.

At about 1900°-2100°F, the glassy ceramic begins to crystallize into β-SiC with minor weight losses (due to residual hydrogen and siloxane groups) along with more bulk volume reduction, structural consolidation and porosity creation. Here, each carbon atom is tetrahedrally bonded to four silicon atoms and each silicon atom is tetrahedrally joined to four carbon atoms in the sp^3 hybridized crystal structure. Above this temperature level, the structure continues to undergo gradual consolidation. The strength, modulus, CTE and hardness of a-SiC are expected to be notably lower than that of β-SiC. At about 3500°-3600°, cubic (fcc) β-SiC rearranges into hexagonal α-SiC with negligible volume and weight changes. Rather than consolidation and bulk volume changes, this transition involves rearrangement of the structure from fcc to hexagonal whose crystal cells occupy about the same volume. While the 3000°F heat treatments shown in Figure 2 are expected to fully convert existing glassy a-SiC (low-fired amorphous or glassy SiC) into crystalline β-SiC, the latter 2200° heat cycle shown in-between seal coats 2 and 3 likely converts a portion of the remaining a-SiC, resulting in a dispersion of crystalline β-SiC domains within the a-SiC matrix. Finally, the last couple of seal coats along with PIP cycles 14 and 15 leave the outer portions of each article completely in the glassy state. Thus, the SiC phase for each of the machined articles is expected to consist of β-SiC near their cores (closest to the fibers and carbon matrix) with increasing a-SiC character toward the periphery and 100% a-SiC at the surface, resulting in a pseudo-functional gradient-type converted matrix.

Now SiC provides excellent oxidation protection up to about 3000°F depending on the level of open porosity which determines the amount of surface area that is exposed. At around 2000°F, surface oxidation is thermodynamically favored and results in the rapid formation of a thin film of glassy (vitreous) silica[2]. Above about 2100°F, the SiO_2 film thickens and densifies resulting in slower oxygen diffusion (through the film) and thus, a slower oxidation rate. Above about 3000°F, interfacial reactions between the SiO_2 film and the SiC substrate become significant, resulting in the formation of volatile SiO and CO. These gaseous products tend to rupture the SiO_2 film, opening up new channels for more oxygen to diffuse in . . . and oxidation continues. The melting point of SiO_2 varies from about 2900° to 3100°F [3] depending on the particular polymorph or structural form. Crystalline forms such as quartz and cristobalite possess melting points near the upper range while amorphous structures will liquefy near the lower end. At elevated pressures, the melting point of SiO_2 likely increases according to the Simon equation[4] which implies that any SiO_2 present in a motor environment may liquefy at higher temperatures than expected . . . $a\left(P - P_{tp}\right) = \left(T_m - T_m^{1atm}\right)^b - 1$

[1] Limited information is available concerning possible mechanisms for carbosilane pyrolytic conversion. These statements are strictly the author's perception.

[2] For SiO2, the terms 'amorphous', 'glassy' and 'vitreous' are all taken to be synonymous.

[3] Approximate values taken from the Handbook of Chemistry and Physics, CRC Press, 60th Edition

[4] F. E. Simon and G. Glatzel. Z. Anorg. u. Allgem. Chem., volume 178, number 309, 1929

where P is the pressure, P_{tp} is the triple point pressure, T_m is the equilibrium melting point at pressure P, T_m^{1atm} is the melting point at 1 atmosphere pressure, and a and b are regression constants. However, impurities in the SiC phase (which inevitably become incorporated into the oxide) will tend to lower the melting point, counteracting the Simon effect. The exact melting point of SiO_2 in the ACM valve environment cannot be ascertained at this point.

In an oxidative environment, the scenario might be described in the following manner. Reaction A – At moderate temperatures, a layer of passive SiO_2 develops on the SiC surface which provides high temperature oxidation protection. The SiO_2 formed is a thin, dense (nonporous), vitreous film of SiO_2. The SiO_2 film/reaction grows inward as it consumes the outer molecular layers of the SiC substrate producing a carbon rich interface. Reaction B – At higher temperatures, interface reactions between the oxide and the substrate commence which induce degradation of the oxide and increase oxygen access to the interface region. Reaction C – As the overall level of oxidation exceeds that of oxide replenishment, oxidation converts from 'passive' to 'active' as exposed SiC surfaces begin to degrade. Reaction D – Of course, any exposed carbon surfaces will rapidly undergo oxidative decomposition at elevated temperatures (only about 550°-600°F is needed to begin oxidation of PAN fibers).

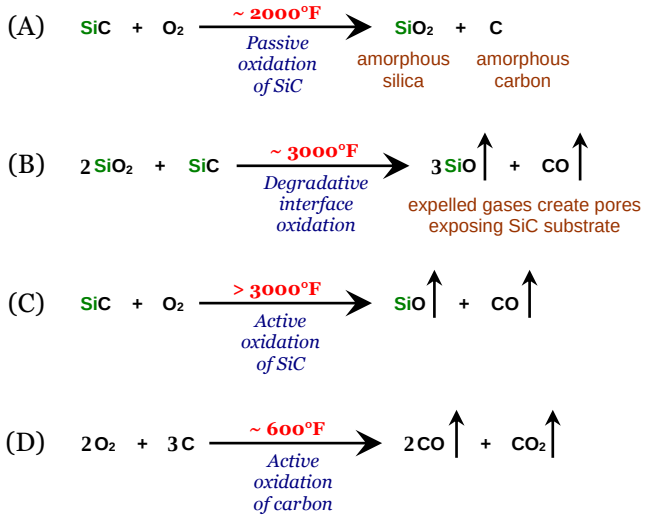

It is customary to approach the kinetics for these types of processes which involve oxide growth, surface conversion and substrate recession by formulating the 'parabolic rate law', $x^2 = kt$, where x is the thickness of the growing oxide (or equivalently, recession of the substrate), k is the rate constant (often evaluated in terms of the diffusion coefficients by assuming a steady state flux or flow process across the air-oxide-substrate interface zone), and t is the oxidation time. This law has proven beneficial for cases having very long durations under the premise that steady state assumptions apply and that the relevant reactions are in equilibrium throughout the process (however, these assumptions may not always be entirely valid in rapid motor fire situations). Oxidation processes that have very short durations, on the other hand, may be modeled by a simpler version of this law which gives the recession/thickness change as linear function of the time. A hybrid of these two approaches, known as the paralinear kinetic model, has been shown to produce good results, specifically for SiC-SiO_2 systems[1]. It might be suggested that a generalized 'power rate law' be formulated such as, $x = k_O t^n$ where $n = 1/2$ for parabolic oxidation, $n = 1$ for linear oxidation and so on (n may be tailored for the specific situation and assume non-integer values). The oxidation rate constant k_O (in units of $(\mu / s)^{1/n}$ for this version) can be taken as a measure of the reactivity of the substrate material to the particular oxidation conditions under study, while n is indicative of the resistance to diffusion/transport associated with the oxide layer (the lower the value of n, the higher the diffusion coefficient).

[1] K.L. More, P.F. Tortorelli, M.K. Ferber, L.R. Walker, J.R. Keiser, W.D. Brentnall, N. Miriyala, and J.R. Price, "Exposure of Ceramics and Ceramic Matrix Composites in Simulated and Actual Combustor Environments," J. Eng. Gas Turbines and Power, 122 212-18 (2000).

The rate 'constant' k is probably not constant but a function of various conditions that influence the oxidation process in a fashion that is either complimentary or impeding. For instance, the temperature dependence might be incorporated in this manner . . . $x \sim K_T e^{-Ea/RT} \cdot t^n$ where K_T is a function of A (the pre-exponential factor), k_O (pure oxidation factor), plus all other factors/conditions that may affect the reaction process. Now in anhydrous oxidative conditions, the amorphous silica does not undergo devitrification or crystallization even at high temperatures. However, if an influential level of water is present in the flame, a crystallized silica phase may indeed develop. It has been confirmed[1] that in the presence of water vapor, a thick, porous, non-protective layer or scale of cristobalite (crystalline silica) forms on top of the thin vitreous silica passivation layer. The presence of water apparently enhances or accelerates the oxidation process presumably by exhibiting its own oxidative power which leads to hydrolytic degradation of SiO_2 into volatile hydroxysilane compounds. In actuality, the volatilization of silica limits the oxidation protective capability of SiC by eliminating SiO_2 from the SiC surface (the more water there is in the flame, the faster SiO_2 is destroyed). Any exposed carbon surfaces will also undergo hydrolytic oxidation thus decomposing the carbon substrate into its volatile oxides. For a flame mixture containing O_2/H_2O, thermal hydrolytic oxidation is the primary degradation mechanism at work, and this combination is more devastating than just oxygen alone. Representative reactions for hydrolytic degradation of C-C/SiC are given below.

(E) $2\,SiC + 3\,H_2O \xrightarrow{\sim 2000°F} SiO_2 + 3\,H_2\uparrow + CO\uparrow$

Hydrolytic oxidation of SiC

(F) $2\,SiO_2 + 3\,H_2O \xrightarrow{\sim 2000°F} HO{-}Si(OH)_2{-}OH\uparrow + HO{-}Si(=O){-}OH\uparrow$

Volatilization of Silica (Hydrolysis)

hydroxy / oxy – silanes

(G) $2\,C + 3\,H_2O \xrightarrow{\sim 1500°F} CO\uparrow + CO_2\uparrow + 3\,H_2\uparrow$

Hydrolytic oxidation of C (Water Gas Reaction)

Now if hydrogen were present in the flame mixture, many of these oxidation reactions may be subdued or counter-balanced considering the strong reducing power of H_2. However, at high hydrogen levels, both SiC and its oxide are subject to etching effects which can also lead to volatilization by converting the siliceous materials into basic silanes and hydrocarbons. . .

(F) $SiO_2 + H_2 \xrightarrow{\sim 3000°F} Si_nH_{2n+2}\uparrow + H_2O\uparrow$

Reduction / etching of SiO_2 (Volatilization)

(G) $SiC + H_2 \xrightarrow{\sim 3000°F} Si_nH_{2n+2}\uparrow + C_nH_{2n+2}\uparrow$

Reduction / etching of SiC (Volatilization)

A similar reaction could be written for the volatilization of exposed carbon surfaces into methane and associated aliphatic hydrocarbons. In a hot H_2/H_2O environment, carbon degradation would not only produce aliphatics, but could possibly lead to the synthesis of complex oxygen-bearing compounds.

[1] P.F. Tortorelli, K.L. More, "Effects Of High Water Vapor pressure On Oxidation Of SiC At 1200°C," Metals and Ceramics Division, Oak Ridge National Laboratory.

Effective densification of porous substrates requires interconnectivity of the pore network and openness to the outside. In large bulk bodies, the intruding fluid must pass through the substrate's outer porosity to reach the inner porosity. Generally, for large panels and substrates, there will be a gradient of resin (or matrix) distribution from the outside to the inside as pores and voids near the center of the billet tend to become closed off or sealed during the first couple of impregnations. Unfortunately, these closed pores and voids often remain impervious from subsequent densification cycles from that point on. In addition to the particular composite molding configuration employed (or specifically in our case, the particular preform weaving and rigidization techniques used), the combination of pore/void interconnectivity and openness is usually a function of the size of the panel or billet. Thus, the larger the billet, the more difficult it is to densify the inner porosity, and the more nonuniform the billet density becomes throughout its volume . . . and it is well substantiated that the composite bulk density is almost directly proportional to most of the mechanical properties. With a high density matrix such as SiC, uneven pre-ceramic resin distribution can have substantial effects on the final composite density. Also, depending on the orientation of the billet when it is placed in the impregnation chamber, gravitational forces can influence the resin distribution causing it to shift from the top to the bottom.

Observation of images from XYZ's impregnation/densification procedure and sample/article lay-out (see Figure 7[1]) indicates excellent cross-sectional intrusion of resin into the substrate with no apparent evidence of unbalanced resin distribution from the periphery to the core. According to [1], the rigidized preform billet is cut into three slabs prior to the densification process. Sectioning into slabs improves resin distribution into the material overall as opposed to processing the entire billet whole.

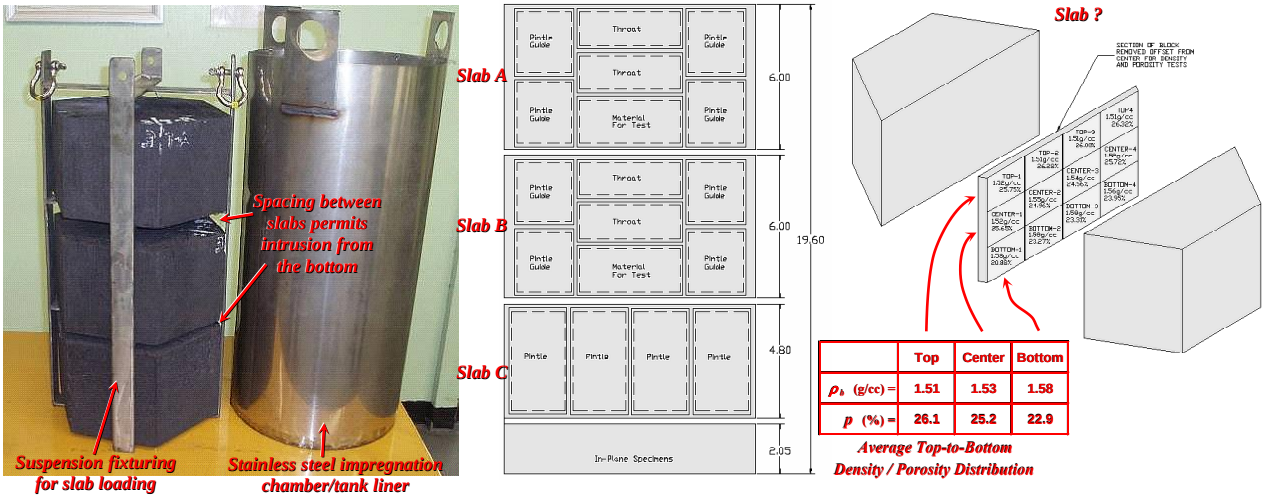

Figure 7. Composite of images and data from the presentation, "XYZ Ceramic Matrix Composite System" for the Orion LAS ACM illustrating slab fixturing prior to impregnation along with article machining lay-out and bulk density / open porosity distribution for one of the slabs after five

However, top-to-bottom distribution for one or all of the slabs in this process may have been influenced by gravitational effects causing slightly more resin to settle in the lower regions. This gravitational distribution gradient could be a result of the particular orientation of the slabs during the process. Perhaps the three slabs were stacked in the same top-to-bottom order in all or most of the densification cycles; or they were placed in the impregnation chamber with the bottom side down in one or all of the impregnation cycles; or cured in the autoclave/cure chamber with the bottom side down in one or all of the impregnation cycles; or allowed to soak in the chamber for long durations during one or all of the cycles while the resin viscosity increased or begin to stage, . . . or a combination of the above.

[1] Data and information taken from the presentation, "XYZ Ceramic Matrix Composite System" for the Orion LAS ACM. Information, illustrations and formats may be simplified, enhanced or reduced to fit the objectives of this discussion without loss in accuracy or correctness.

Development of composite physical properties across the densification process occurs incrementally as the substrate is subjected to each PIP cycle consisting of impregnation with resin (or resin/particle slurry), autoclave cure and then 1550° pyrolysis. After the 5th and 10th cycles, the slabs are subjected to a 3000° heat treatment cycle which crystallizes the glassy SiC matrix. Composite densities, matrix content (and matrix volume) and most mechanical properties are increased substantially after the first few cycles and then gradually taper off after that. This trend is depicted in Figure 8 which shows bulk density evolution for one of the C/C-SiC slabs [1] (the two heat treatment steps applied are indicated).

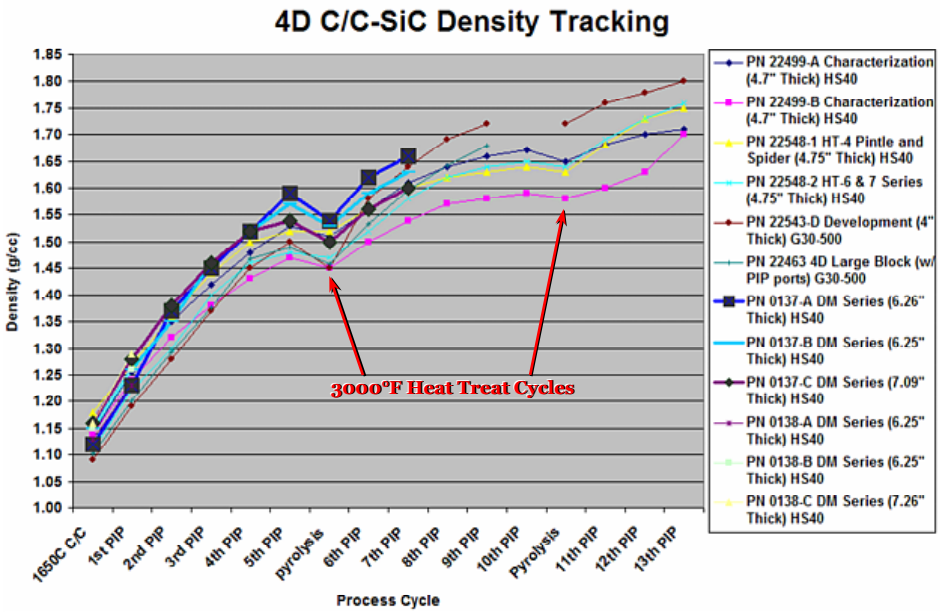

Figure 8. Cumulative increase in composite bulk density as various preform slab sections were processed through XYZ's CMC densification process. Taken from the presentation, "XYZ Ceramic Matrix Composite System" for the Orion LAS ACM.

This trend is typical of CMC and C-C materials undergoing sequential densification processing. Many studies have demonstrated similar behavior for most of the critical constituent properties and some of the mechanical attributes as they progress across the densification process including composite bulk density, true density, matrix content, matrix volume, fiber content, flexural strength and interlaminar (or interlayer) tensile strength. Moreover, this behavior has been shown to exhibit a functional component and can also be defined in terms of substrate impregnation weight gains and pyrolysis weight losses[2]. Experimental validation has confirmed that functional (analytical) descriptions of these properties tend to follow exponential (response function) type characteristics asymptotically approaching their maximum (or minimum) value as they change across the densification process. Indeed, using the data given in Figure 8, unique model curves can be developed for each of the three segments of any of the slab articles . . . from the C/C state through the first 3000° heat treat after the 5th PIP, and from that point to the second heat treat after the 10th PIP, and then from there on out. Specifically, the evolution of constituent properties P for any given segment as well as over the entire densification process can be precisely tracked with a generic response function of the form . . .

$$P = A\left(1-e^{-ki}\right) + C$$

where i is the densification state (or cycle), $C = P_0$ is the initial value of the property P at $i = 0$ (the carbon state) and $A = P_{\max} - P_0$, which brings clarification to the more descriptive form . . .

$$P = \left(P_\infty - P_0\right)\left(1-e^{-ki}\right) + P_0$$

[1] Data and information taken from the presentation, "XYZ Ceramic Matrix Composite System" for the Orion LAS ACM. Information, illustrations and formats may be simplified, enhanced or reduced to fit the objectives of this discussion without loss in accuracy or correctness.

[2] Derivation and proofs for such concepts have been personally substantiated and long established – Consult the Appendix for in-depth clarification.

Consider data specifically for the 22499-A slab section shown in Figure 8. While a more precise evaluation of the data could definitely be established by evaluating each of the three densification segments individually, pre-trials have indicated that treatment of the entire data set as one continuous densification process is sufficient for the current discussion in demonstrating the validity of this approach (more elaborate treatments of the individual segments can be pursued at a later time if necessary). Figure 9 gives a consolidated plot of the data for article 22499-A as extracted from the density data in Figure 8 along with the average model curve fit.

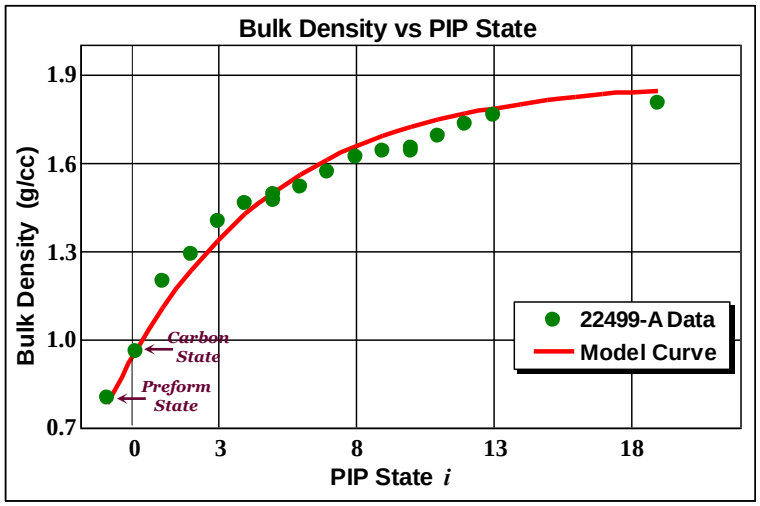

Figure 9. Plot of density data for slab section 22499-A extracted from Figure 8 with overlay of the average model curve fit.

For the 22499-A slab, the final (average) bulk density is known to be 1.80 g/cc, that of the dry preform was 0.8 g/cc, and 0.96 g/cc after the pitch carbon densification step[1]. The functional description for the bulk density of the 22499-A slab based on this data was determined to be best represented by . . .

$$\rho_b \cong 0.92\left(1 - e^{0.18i}\right) + 0.96$$

where $\rho_{b,0} = 0.96$ g/cc is the bulk density of the slab after pyrolysis of the mesophase pitch fraction and ρ_b approaches an average of . . . $0.92 + 0.96 \cong 1.88$ g/cc after an infinite number of SiC densification cycles (if that were possible).

Now the density of HS40 fiber is given as 1.85 g/cc [2] and since $\rho_b = f_v\rho_f + m_v\rho_m$, [3] the initial fiber volume fraction of the dry (undensified) preform can be estimated. Recall this structure has not yet received any densification treatments and thus contains zero matrix (other than the rigidization coating which is unknown at this point but presumed to be insignificant for this analysis). Using the dry preform bulk density of 0.8 g/cc, the fiber volume fraction comes out to be . . .

$$f_{v,P} = \rho_b / \rho_f = 43.24\%$$

It is safe to assume this value does not measurably change throughout the entire densification process and so the original fiber volume fraction is the same as the final fiber volume. Now the matrix weight fraction is also given by . . . $m_w = 1 - f_v\rho_f / \rho_b$, whose only variable (in this particular relation) is the composite bulk density. A plot of the matrix content (as a function of the bulk density data from Figure 8) is given in Figure 10 below along with its model curve which, as with the bulk density functional fit, is intended to be representative of the matrix content across the entire spectrum.

[1] Information acquired from independent or undisclosed sources.

[2] Consult [1] on page 2.

[3] Consult the Appendix of this report for elaboration on the development of this approach and justification of its use.

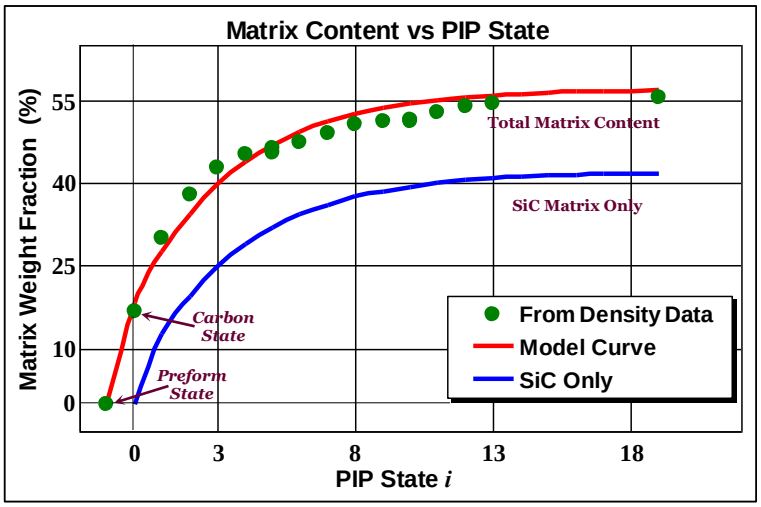

Figure 10. Plot of the matrix content based on bulk density data for slab section 22499-A with overlay of the average model curve fit.

This analysis implies an carbon matrix weight fraction in the range 17-19% deposited from the initial pitch densification step which remains unchanged from that point on. Matrix fractions in these kinds of composites are extremely difficult to physically measure and so an estimation technique such as this can sometimes prove beneficial during design and characterization processes. Now the average functional description for the Total Matrix Content in the 22499-A slab was determined to be . . .

$$m_w \cong 38.6\left(1 - e^{0.27i}\right) + 18.5$$

where $m_{w,0} \cong 18.5\%$ is the carbon matrix content after pyrolysis of the mesophase pitch fraction and the total m_w approaches 57.1% after an infinite number of SiC densification cycles (if that were possible). A similar scenario could be developed for the SiC portion of the matrix which tops out at around 41-42%.

Now as the substrate density increases over the process, the open porosity decreases as it gradually becomes occupied with matrix material. While other properties are represented by increasing functions, the porosity decreases in an inverse manner. Evolution of the porosity volume fraction can be explored in a likewise manner by applying the following formula [1] . . .

$$p = 1 - f_v - m_w \rho_b \rho_m^{-1}$$

However, the matrix density is a complex combination of the carbonized pitch, crystalline (β) SiC and amorphous SiC (these two SiC densities are *not* identical), but a rough estimate can be surmised by making note of the various fractions for each matrix component and the approximate densities. Green (amorphous) coke has a density of about 1.3 (far from the crystalline order of pure graphite whose x-ray density is 2.25); for this case, the density of crystalline β-SiC is taken as 3.0 (pure electronic grade β-SiC has an x-ray density of 3.22, but the SiC in these articles is known to contain carbon as well as other impurities and defects); amorphous SiC (especially the form derived from SMP-10) has been reported to have a density of about 2.4[2]. Using Figure 2 as a reference, the matrix fraction is considered to be comprised of about 17% a-C, 58% β-SiC and 25% a-SiC, which gives an approximate composite matrix density of about . . .

$$\rho_m = \left(0.17\rho_{a\text{-}C}^{-1} + 0.58\rho_{\beta\text{-}SiC}^{-1} + .25\rho_{a\text{-}SiC}^{-1}\right)^{-1} = 2.33 \text{ g/cc}$$

A plot of the 22499-A open porosity throughout the densification process (as a function of the original bulk density data from Figure 8) is given in Figure 11 along with the model function representing the open porosity of the substrate across the entire densification domain and beyond.

[1] Consult formula 2A in the Appendix of this report for elaboration on the development of this approach and justification of its use.

[2] Information acquired from independent or undisclosed sources.

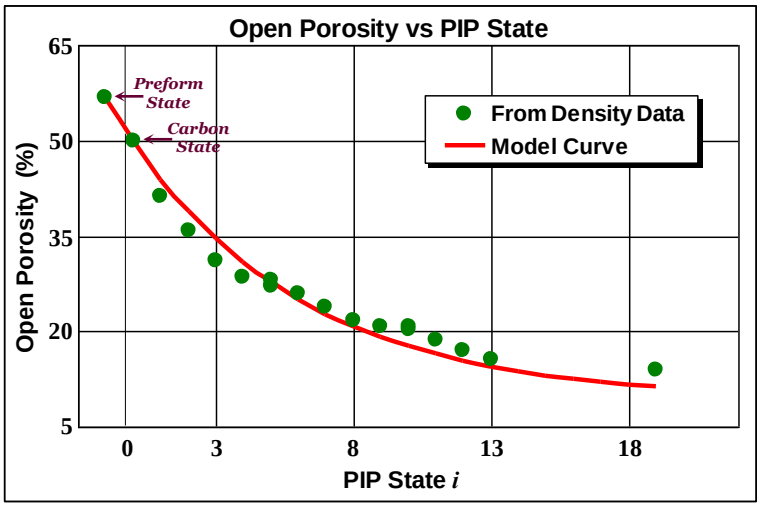

Figure 11. Plot of the open porosity based on bulk density data for slab section 22499-A with overlay of the average model curve fit.

Behavior of the porosity fraction is almost the exact converse of that for the bulk density because as the SiC matrix fills the porosity, the bulk density increases accordingly. The optimized functional description for the open porosity of the 22499-A slab as it progresses through the densification process has been determined to be . . .

$$p \cong 40.6\, e^{0.16i} + 9.3$$

The initial porosity of the dry woven preform is simply $1 - f_v = 56.8\%$. After the pitch densification cycle, the slab/substrate porosity is estimated to be $p_0 = 40.6 + 9.3 = 49.9\%$, and after unlimited densification cycles (if it were possible), the porosity would approach an average of $p_\infty = 9.3\%$.

The true or real density of a composite is the density of the non-pervious portion of the material, that is . . . $\rho_t = \rho_b / (1 - p)$. [1] It is the bulk density less the influence of the porosity fraction, or the combined density of just the fiber and matrix. It is always higher than the bulk density. Relationships between these densities and the open porosity for the 22499-A slab are illustrated in Figure 12.

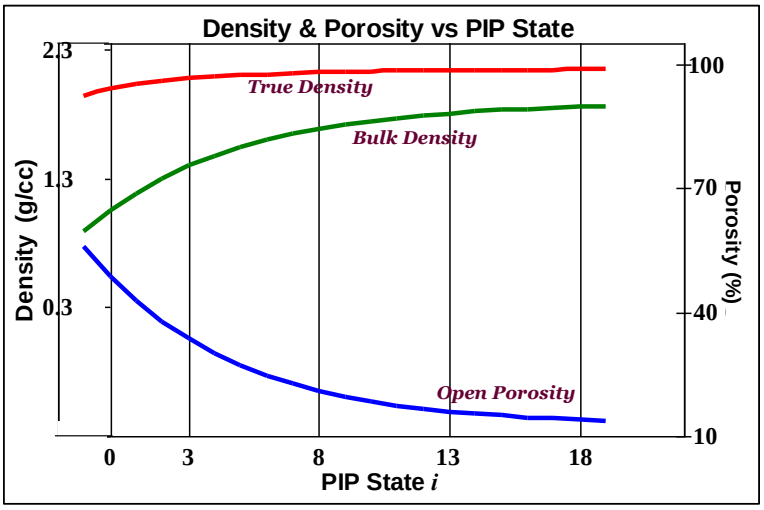

Figure 12. Model curves for the bulk density, true density and open porosity for the.22499-A slab.

[1] Consult the Appendix of this report for an explanation and more elaborate definition of this and other concepts developed in this section.

True density is sometimes a measure of fiber-to-matrix binding and has been shown to heavily influence mechanical attributes in such tests as flexural, interlayer shear, interlayer tensile, longitudinal compression and differential CTE (in the longitudinal direction). Since the bulk density includes the porosity fraction, it will tend to have a attenuating effect on mechanical and thermal conduction as well as shock propagation and vibrational damping. However, it will also affect (negatively) the same properties given above because higher levels of pores and voids will reduce fiber-to-matrix contact area.

Now an expression defining the evolution of the matrix content across the ceramic densification process can be derived in terms of the impregnation weight gains and pyrolysis weight losses. However, FMI holds the records for this data. In lieu of the slab weight changes, matrix content estimation can be formulated in terms of state-to-state substrate densities using the data depicted in XYZ's chart of Figure 8 and Eq(5A) developed in the Appendix (see the Appendix for derivation of all expressions, nomenclature and notation used in this discussion). With this simplified formula, the total matrix content m_w can be computed for each of the ceramic states i throughout the process starting with the dry preform state P and progressing across all the subsequent states, $i = 0,1,2,3,...$

$$m_{w,i} = 1 - \prod_{P}^{i} \rho_{b,i-1} / \rho_{b,i}$$

As expected, the set of values derived from this expression are an exact match for the plotted values and the model curve already produced in Figure 10 for the total matrix content. This approach opens the door to precise characterizations of all the other material constituents based solely on measured bulk densities (or impregnation/pyrolysis weight changes). Constitutive representations for matrix volume fraction, fiber weight fraction, ceramic weight gain, matrix density, flexural strength and interlayer strength are sometimes only vague perceptions the manufacturer/designer wishes they had a better hold on.

It might be noted that all of the preceding results developed in this discussion represent average, overall properties for the entire slab, and it should be realized . . . each property will inevitably vary from one point in the substrate body to the next. Both 2-D and 3-D composites are highly anisotropic, non-homogeneous materials. By their very nature, the non-uniformity and anisotropy characteristics of composite materials are not only inherent by design, but are also governed by a host of manufacturing parameters and process conditions which influence the distribution of material properties throughout the body, and many of these variables are beyond the manufacturer's control (unfortunately). Thus, this analysis cannot necessarily detect nor fully address the spot-to-spot variability that likely played a role, to some degree, in the recent HT-5 and HT-7 failures.

If the preceding analysis were broken down further and a more detailed evaluation was performed to account for the two 3000° heat treat steps, all of the previous values and functional results given above would shift (slightly). As a matter of fact, if additional heat treat cycles were applied to the material across the process, more of the open porosity could be densified and reduced perhaps down close to the 3-5% level, but the exact ramifications of this porosity level on the performance properties of the final product in the ACM application cannot be ascertained at this time. It should be realized that since each pyrolysis creates new pores and voids, a final porosity of zero is impossible – the bulk density will never reach the true density and the two will never coincide.

It should also be noted here that the final average porosity of ~13% as reported by XYZ for these articles is not the total porosity fraction of the composite but pertains to the 'open' porosity, that is, the fraction of pores, voids and cavities that are accessible to intruding fluids. The porosity and densities values given in Figures 7 and 8 were measured by an Archimedes-type technique using water or solvent which generates an apparent or 'open' porosity fraction and associated bulk density. The apparent 'true' composite density is estimated from these values and, most importantly, the level of 'closed' or sealed porosity is completely unknown.

What is known however, is that the inaccessible fraction of the total porosity fraction for these types of 3-D composites can be quite substantial, sometimes double the level of the measurable open porosity. For instance, a significant level of closed cavities in C-C/CMC composites is known to exist in the interstitial regions around fiber bundle intersections of the weave structure (this topic will be further explored in the next section regarding the HT-7 C-C/SiC failures). The effects of moderately high levels of both open and closed porosity can be either beneficial or detrimental depending on the end application with respect to the mechanical and thermal expectations. Obviously, high porosity levels in a composite will adversely affect its structural and ultimate strength capabilities, but will reduce thermal conduction through the composite (if that was a desired feature) and may tend to subdue potential failure mechanisms associated with thermal and mechanical shock incursions.

Analysis

In ordinary 2-D unidirectional lamina with much higher longitudinal fiber volume fractions, longitudinal tensile properties are overwhelmingly fiber-dominated, while matrix attributes (and fiber-to-matrix bonding) typically dominate composite properties in the transverse (interbundle) and interlaminar directions. However, with the HS40 C/C-SiC material produced by FMI, any given direction of orientation can be expected to contain an appreciable level of matrix dominance. Matrix co-dominance in the HS-40 composite is a result of the low fiber volume along with particular attributes associated with the multi-phase matrix that are incorporated into the pore structure of the preform throughout the densification process. As such, its mechanical properties are determined, to a substantial degree, by the properties and behavior of the C/SiC matrix, whose primary function traditionally is to bind the fibrous phase together. The condition is reflected in Table 1 which contains tensile and compression test data for fully densified, coated material from the 22499 slab provided by FMI[1].

Material Characterization
HS-40 4D C/C-SiC
1 cycle low graph
P/N 22499

Test Type	Sample Orientation	Test Temp, °F	Failure Stress, ksi	Elastic Mod, msi	Failure Strain, %	Bulk Den, g/cc	Porosity %
Tension	U Direction	72°F	24.5	6.77	0.387	1.78	14.07
		2000°F	20.8	7.34	0.293	1.79	13.54
		4000°F	20.4	4.56	0.500	1.81	12.72
	U+90 Direction	72°F	14.3	5.99	0.349	1.77	14.01
		2000°F	17.5	4.54	0.443	1.75	15.37
		4000°F	16.2	3.39	0.653	1.75	15.27
	Z Direction	72°F	20.1	10.2	0.200	1.82	13.23
		2000°F	19.6	10.8	0.184	1.82	13.30
		4000°F	18.1	5.23	0.365	1.79	14.54
Compression	U Direction	72°F	33.5	7.39	0.479	1.81	12.58
		2000°F	40.4	7.74	0.574	1.84	11.48
		4000°F	33.5	3.31	1.500	1.84	11.59
	U+90 Direction	72°F	23.2	6.25	0.555	1.84	11.65
		2000°F	32.3	6.63	0.490	1.84	11.74
		4000°F	29.7	3.03	2.025	1.85	11.32
	Z Direction	72°F	42.8	9.5	0.468	1.82	12.14
		2000°F	42.9	9.3	0.626	1.80	12.84
		4000°F	43.0	5.09	2.310	1.83	11.77

Table1. Tensile and compression test data for the 22499 HS-40 C/C-SiC slab taken from "XYZ Ceramic Matrix Composite System" for the Orion LAS ACM

[1] Data and information taken from the presentation, "XYZ Ceramic Matrix Composite System" for the Orion LAS ACM. Information, illustrations and formats may be simplified, enhanced or reduced to fit the objectives of this discussion without loss in accuracy or correctness.

While the complete mechanical test set also contained other results, particular trends reflected in these two data sets are worth noting (a full analysis of their data is not the intent of this section). Historically, studies have indicated that carbonized PAN fibers (and their composites) tend to drop in tensile strength as test temperatures are increased, while the polymorphs of SiC are well known for their strength retention or slight elevation at high temperatures.[1] This means that the matrix plays an ever-increasing role in the properties of SiC-densified systems as the temperature goes up. It should be emphasized that testing at only these three temperatures is inadequate for a true understanding of what is going on here, which tends to make most attempts to explain the phenomena taking place little more than speculation. However, consider first the general mechanical differences between the three test directions *u*, *u*+90 and *z*, disregarding their temperature-to-temperature variations for the moment. If necessary, make reference to Figure 1 on page 2 and the associated discussion on pages 1, 2 and 3.

Tensional loading along the *z* direction is obviously contingent on the fiber tensile properties but the actual level of loading required for failure is wholly dependent on the volume fraction of continuous, longitudinally oriented fibers in the *z* direction (recall that the measured tensile strength for HS40 fiber bundles is 670 ksi). At a secondary level, fiber bundles that are perpendicular to the *z* axis (i.e... the *u, v* and *w* layers) will tend to undergo interlayer tension (or bundle separation) which is entirely dependent on fiber-to-matrix bonding properties. These forces are acting to pull the *u, v, w* planes away from each other, however, since there are no weave interlacings connecting bundles in the same plane together, single out-of-plane and interbundle separations can also result (i.e... the *u*, *v*, *w* planes are not unique; each is just a series of parallel non-connecting fiber bundles in the same plane). Thus, *z* axis tensional loading is probably dominated by longitudinal fiber properties while secondary loads are placed along the fiber-matrix interfaces comprising the *u, v, w* interlayer stack-up perpendicular to the loaded *z* axis.

Similarly, tensional loading along the *u* direction is also contingent on the effective *u*-oriented fiber volume but this is coupled with longitudinal contributions from the off-axis *v* and *w* fiber bundles which will increase the stress required to fail the material over that required for the *z* direction. This is reflected in the data of Table 1. Off-axis loading of the *v* and *w* layers in both the *u* and *u*+90 direction will be associated with interbundle tension and shearing between *u, v, w* bundle surfaces in contact with perpendicular *z* bundles, which is again, dependent on fiber-to-matrix bonding properties. However, the *u* + 90 direction has no direct (axial) longitudinal fiber contribution and is even lower than the *u* and *z* directions. This is also reflected in Table 1. Thus, fiber-to-matrix interface bonding plays a secondary but significant role in tensional loading in all three test directions. In all three cases of course, the tensional properties of the matrix itself plays either a secondary or tertiary role in the loading or failure process. In short, tensional loading along the *z* and *u* longitudinal directions is probably fiber-dominated, albeit slightly. while *u*+90 loading is dominated by the matrix (and/or fiber-to-matrix bonding).

The compressive strength of SiC is many times that of carbon fibers and it is expected to dominate compressional loading in all directions. However, the fiber bundles do play a secondary role. Compressional loading in the *z* direction will tend to buckle the *z* bundles while interlayer compaction of the *u, v, w* planes begins to take effect (into-plane bundle-to-bundle compression). Buckling of *u* bundles is also predominant when loading is oriented in the *u* direction. This is also accompanied by interbundle compression and shearing between *u, v, w* bundle surfaces in contact with perpendicular *z* bundles causing interbundle compaction along with interbundle shear, the latter of which is highly influenced by fiber-to-matrix bonding properties. These same forces are also at play during *u*+90 loading except that there is no direct longitudinal fiber component, which tends to make the *u* + 90 direction the weakest of all three (in both tension and compression). These descriptions are clearly reflected in Table 1. As with tensional loading, the effective fiber volume fraction in the longitudinal *z* direction significantly affects the ultimate magnitude of failure. In all three cases however, the compressional properties of the SiC matrix dominate the loading process. When the matrix finally fails in compression, longitudinally oriented bundles will undergo buckling, often with a 'brooming' effect.

[1] Information acquired from multiple, unknown or undisclosed sources.

Fiber-to-matrix bonding is most pronounce in multi-modal loading situations such as flexure in which significant shear forces are at play. It is now apparent that shear forces are significant contributors in almost all directions of loading. The fiber-to-matrix interface can be developed by both chemical bonding and physical interactions (recall the discussion at the top of page 7 covering fiber-matrix bonding concepts). Fiber surface functional groups (such as acyl and carboxyl) may tend to repel the highly aromatic pitch material at first but after pyrolysis, these groups form strong coupling links with carbonized matrix atoms via free radical mechanisms. An analogous mechanism likely leads to bonding interactions with carbon atoms in the SiC phase (see Figure 13[1]), and considering the high level of ceramicized SiC matrix in the composite, establishment of strong bonds at the fiber-to-SiC and carbon matrix-to-SiC interfaces will be substantial. Physical bonding comes about due to the surface porosity, roughness and specific contours of the interfaces. It is expected to play a significant role in the overall bonding scenario joining the fiber surfaces to both the carbon and SiC matrix phases.

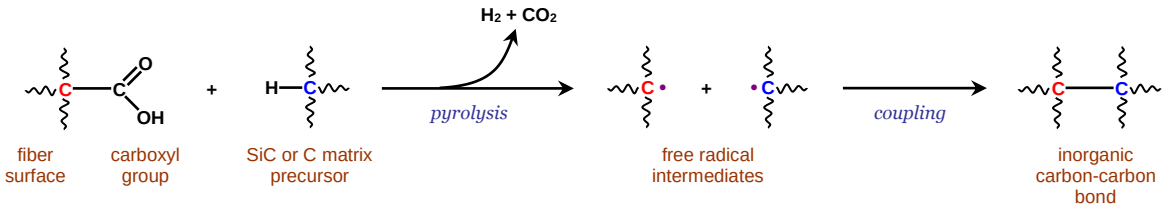

Figure 13. Free radical coupling between a fiber surface functional group and carbon atom during pyrolytic conversion of the matrix.

Another point of interest reflected in the data of Table 1 concerns the trend in strength values from room temperature to 2000° to 4000°. The data indicates the following conditions . . . (1) In the *u* and *z* tensional directions, strength and modulii values decrease as the test temperature is increased; (2) In the *u*+90 tensional direction, as well as the *u* and *u*+90 compressional directions, strength values are higher at the 2000° test temperature and then drop back a little at 4000°; (3) The *z* compressional values remain about flat throughout; (4) Drastic increases in strain-to-failure values and large reductions in modulii are apparent at the 4000° test temperature for all orientations across the board. As the preceding discussion has inferred, the influence of longitudinal fiber contributions is significant, especially at lower temperatures where the balance between fiber dominance and matrix dominance tends to favor the fiber in directions with greater longitudinal contributions.

At the higher temperatures however, the relative levels of matrix dominance vs. fiber dominance are shifted in favor of the SiC matrix because strength properties of the fibers decrease with temperature while that of SiC remains or slightly increases at elevated temperatures. Thus, tensional loading in directions already influenced by direct longitudinal fiber contributions, such as those stated in (1) above, apparently maintain a slight balance of fiber dominance as they show consistent decreases in the stress levels across the three temperatures. For the orientations given in (2), minimal contributions from longitudinal fiber projections allow the increasing SiC matrix strength to dominate at the 2000° test temperature while a fairly even balance between fiber and matrix is apparent in (3). Above the 1900°-2100° range however, peripheral a-SiC matrix domains and seal coating layers begin to undergo transition from the amorphous (glassy) state into nano-crystalline β-SiC, that is . . . a-SiC → β-SiC (reference the discussion on page 9 regarding the thermal/conversion behavior of SMP-10).

As regions of a-SiC are transformed into *β*-SiC, porosity creation and volume shrinkage result in reduced fiber-to-matrix contact . . . along with associated reductions in chemical fiber-to-matrix bonding (and matrix-to-matrix bonding between the carbon and SiC phases). The overall loss in bonding strength is not necessarily substantial since matrix shrinkage will also tend to increase physical bonding between phases somewhat by causing the matrix to 'grip' the fiber surfaces better, further modifying the balance between chemical and physical bonding at all the interfaces.

[1] All chemical structures, reactions and descriptions are solely the perception of the author and no guarantee is made regarding their accuracy.

However, declining composite strengths and associated moduli at the 4000° test temperatures are apparent for directions that are the least influenced by direct longitudinal fiber contributions and more dominated by fiber-to-matrix bonding, such as those given in (2) above. High temperature matrix domination in these test directions is a reflection of the strength retention or slight increase that is characteristic of SiC while the small strength losses at 4000° are indicative of reduced fiber-to-matrix (and matrix-to-matrix) bonding. Unfortunately, a precise understanding or substantiation of this behavior cannot be ascertained with only these three test temperatures. The strain values given in Table 1 may also shed light on certain phenomena occurring during thermal expansion of the material. For instance, maximum tensional strains for each of the *u*, *u*+90 and *z* directions are somewhat reflective of those indicated for the thermal expansion test results given in Figure 14 below for the 22499 slab[1].

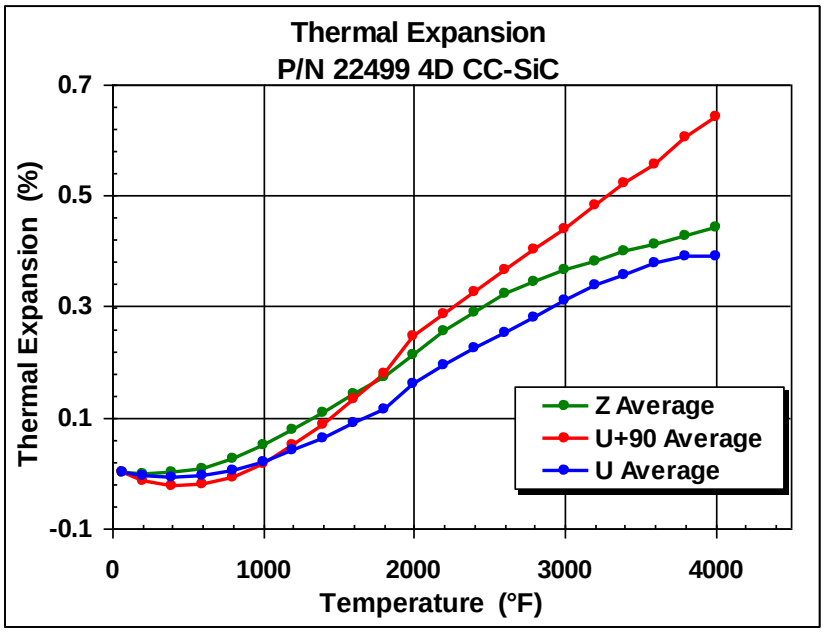

Figure 14. Instantaneous thermal expansion test results for slab 22499 in the three directions under study to 4000°F

Due to the highly anisotropic nature of the 4D C/C-SiC composite system, differential thermal expansion between the fiber, the two SiC phases and the amorphous carbon matrix are expected to have substantial effects on the net expansion behavior in the various orientations. In addition, the directional properties of the constituents play an underlying role in the way the various interfaces interact, and many of these interfaces are often placed under residual stresses by the end of the manufacturing process due to CTE mismatches (usually imparted during cool down steps).

While the fiber exhibits high longitudinal anisotropy, it may be considered, in some respects, to be transversely isotropic across its diameter, However, this viewpoint must be taken with caution since the orientation character of the graphene basal planes is highly dependent on the fiber manufacturing parameters and may vary from point-to-point in a given fiber. The carbonized pitch matrix will tend to have its basal planes oriented in favor of the fiber longitudinal basal directions as it tends to drape across the filament contour, but out farther away from the fiber surface, these basal layers become more like convoluted ribbons in random directions. The a-SiC and *β*-SiC matrix phases might be viewed as structures with disordered and ordered isotropy respectively.

[1] Data and information taken from the presentation, "FMI Ceramic Matrix Composite System" for the Orion LAS ACM. Information, illustrations and formats may be simplified, enhanced or reduced to fit the objectives of this discussion without loss in accuracy or correctness.

From Figure 14, matrix dominance is apparent for the *u*+90 test direction in which no direct longitudinal fiber contributions are involved. Longitudinal fiber expansions are close to zero and are expected to restrain the expansion process in fiber-dominated orientations such as the *z* and *u* directions. Recall that longitudinal HS40 fiber CTE is negligible (as are most PAN-based carbon fibers) while transverse HS40 bundle expansion is around 4-5 or greater (if necessary, reference the discussion on page 2 regarding the thermal properties of HS40 fiber). Note that conversion of peripheral a-SiC into β-SiC around 1900°-2000° is indicated along the *u*+90 curve (also, conversion of β-SiC into α-SiC occurs around 3500°-3600°). In addition to strong longitudinal fiber character in the *z* and *u* directions, projection components for transverse expansion likely play a secondary role in the expansion process for the *u* and *u*+90 directions while direct transverse bundle expansion of the *u, v, w* layers compliments the *z* expansion process. Longitudinal fiber restraint in the *z* and *u* directions is also indicative of strong fiber-to-matrix bonding, especially at the higher temperatures. As with most composites, 'free' expansion may be the prescribed test concept but the constituents often restrain themselves in accordance with the properties of the matrix, the fibrous reinforcement and the nature of fiber-to-matrix bonding.

Another point of interest concerns the surface geometry changes that the article would apparently assume in accordance to Figure 14 as it undergoes expansion. At the higher temperatures, cylindrical surfaces of articles machined parallel to the *z* axis (such as the pintle sides and shaft surface) will tend to exhibit a waviness effect where the contour consists of regular (sinusoidal-like) low spots and high spots corresponding to the *u*/*z* and *u*+90 directions respectively. Coupled with similar features on the pintle guide surfaces (also machined out of the same billet), it is unknown what the combined interference effects might be as the pintle surface moves relative to the guide surface during motor operation. At 3000°, gaps between high points could be as much as a half a percent closer than anticipated, conceivably causing these two surfaces to lock up. This 3-D surface waviness would be purely a function of the weaving configuration, namely, all the fiber-dominated *u*, *v, w* axial orientations in conjunction with all the adjacent, matrix-dominated *u*+90 regions. On the other hand, along the *z* direction of the pintle, expansion would appear to be substantially restrained by the longitudinal fiber CTE coupled with strong fiber-to-matrix bonding, as indicated in Figure 14, .

A detailed analysis of the HT-7 failure was conducted by ATK and a subsequent report issued[1]. In their report, ATK appears to have performed an excellent and comprehensive analysis and all that will be presented in this discussion are observations and comments to supplement their findings regarding the two fractures associated with the pintle article. These comments are not intended necessarily to reveal any new revelations but to make note of details probably already well known by the Launch Abort System (LAS) team. Both fractures occurred on the pintle shaft propagating directly across the shaft diameter, the first apparently at the plane separating the shaft proper from the threaded region and the second at the plane separating the shaft proper from the pintle head. Near the beginning of threaded section, fabricators machined a circumferential u-shaped groove around the shaft which separates the threaded section from the shaft proper (the so-called thread relief groove). Consequently, this became the narrowest diameter region of the entire pintle body and is attributed, in large part, to the reason the failure occurred at this point. While all surfaces on the pintle are comprised of machined fibers, machining of this circumferential groove damaged additional *z* reinforcement fibers around the periphery of the shaft reducing an already low fiber volume fraction even further. Points where *z* bundles are only partially remaining, and even more importantly, *z* bundles that have been completely machined through represent the weakest circumferential regions of the pintle article. It is obvious that more than 5 bundles have been damaged by machining this groove as ATK has suggested[1]. Figure 15[2] gives images of both fracture surfaces for failure #1 along with several notes and a discussion that follows.

[1] Reference the report, "ACM (Attitude Control Motor) High Thrust Test 7 (HT-7), FAILURE INVESTIGATION INTERIM REPORT", May 30, 2008. A final report (if any), supplemental information, data, findings or revisions are unknown at this time.

[2] Images of fracture surfaces extracted from the report, "ACM (Attitude Control Motor) High Thrust Test 7 (HT-7), FAILURE INVESTIGATION INTERIM REPORT", May 30, 2008. These images and the ones that follow were the only ones made available to the author – whether or not further analysis was performed or additional images are available are unknown at this time.

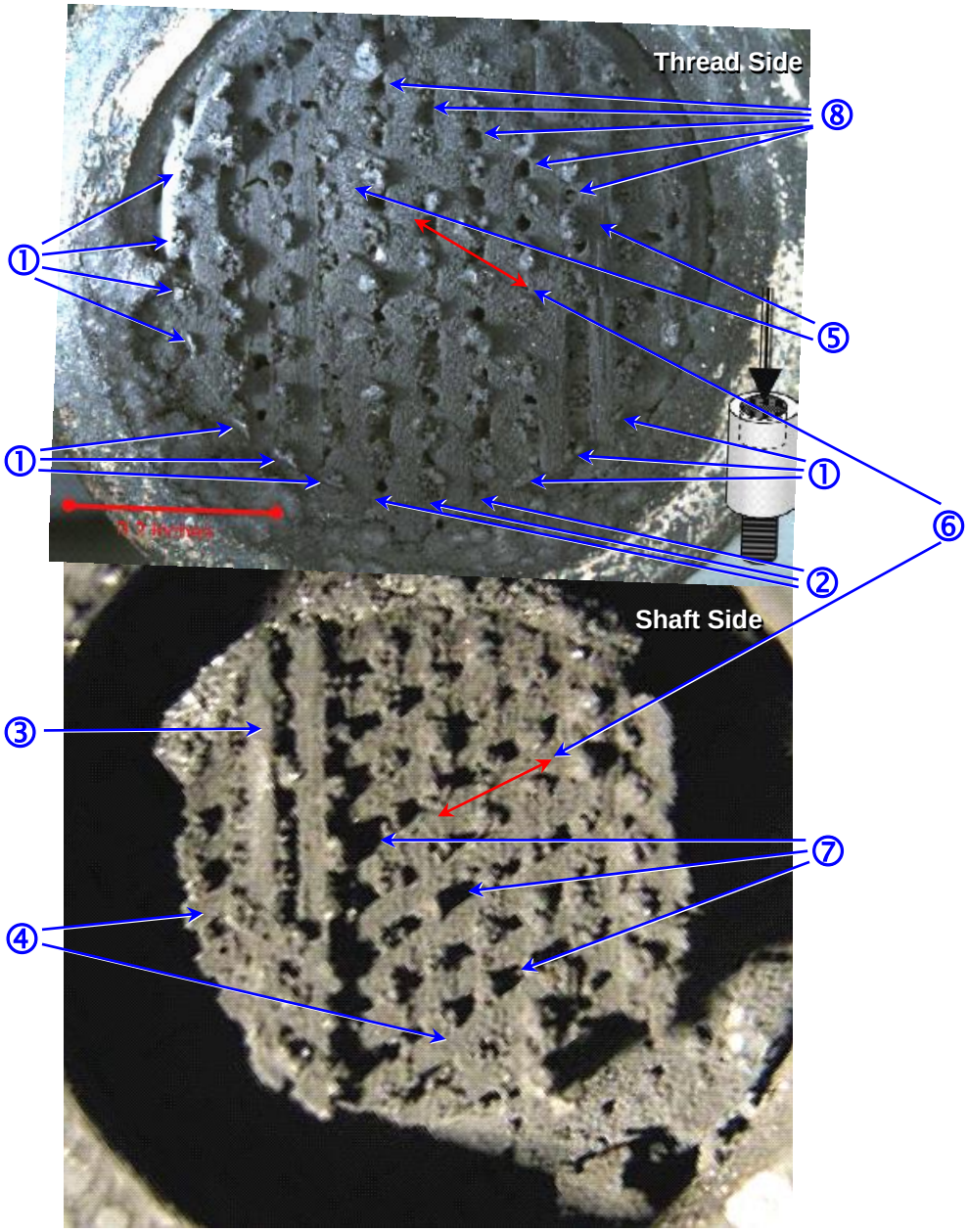

Figure 15. Mating fracture surfaces for the first failure showing characteristics of the C-C/SiC material and features associated with the fracture. These two images were taken from ATK's report at random placement and oriented in this manner to illustrate possible mating correlations between the two surfaces.

As mentioned earlier, the intent of this discussion is not to evaluate the performance of the motor valve but only to comment on some of the features and possible ramifications associated with the fractured C-C/SiC material. In all likelihood, this first fracture did not happen in a single snap but occurred in more than one step. There is no clear evidence that many, if any, of the bundles were liberated here as ATK inferred, rather, most of the features on these two surfaces mate up fairly well . . . considering the fact that both surfaces contain heavy deposits of soot and combustion products and have been obscured by hot gases and extreme temperatures. Without a doubt, an exact match between all corresponding features is less than ideal. However, the following observations and comments can be made relative to the features which are numbered above . . .

① Damaged *z* fiber bundles on the Thread Side that were partially cut through during machining of the groove. These became circumferential weak points.

② Missing *z* fiber bundles that have been completely machined through. Some are next to voids/pores (discussed below). Without a doubt, these are the weakest points on this side of the shaft groove.

③ Pair of bundles on the Shaft Side from a layer arbitrarily designated as the *v* layer which means the layer just below these two bundles as indicated by ④ contains the associated *u* bundles and thus the fracture involved mostly the *u*-*v* interface with a couple of *v* bundles along the *v*-*w* interface. Recall there is no weave interlacing to keep bundles in a given layer directly associated with themselves and so bundles may act independently or in groups at random. It should also be noted that *u*, *v*, *w* bundles near the circumference (edge) are the shortest length bundles in a given layer and thus represent weak regions with respect to interlayer bonding between adjacent bundles.

⑤ Remaining *v* layer bundles on Thread Side. Texturing and directional imprints associated with the *u* layer can also be seen on both faces, ⑥.

⑦ Most of the dark spots on the Shaft Side are not exposed voids or porosity but are shadows cast from the camera flash across the *u* surface due to protruding z bundles. The majority of the protruding bundles seems to occur on the Shaft Side which implies that most of them broke near the *v*-*w* interface on the Thread Side which is also where most of the voids were apparently exposed during the fracture. Thus, these 'holes' are not due to 'fiber pull-out' but resulted from fiber/bundle breakage on the other side of the *v* layer near the *u*-*v* interface where the level of porosity and voids may have been higher than other areas of the substrate for some reason or another. This could have been a result of ineffective resin intrusion into this region or perhaps impermeable pores and cavities that became sealed off early in the densification process.

⑧ Typical exposed voids, pores and cavities associated with *v*-*w* fiber bundle intersections. Note these voids run in the same direction as the *u* bundles. For convenience of reference, when looking from the Shaft Side toward the Thread Side, they can be visualized as being under the *u* bundles. Consider a reproduction of Figure 1 given in Figure 16 below which highlights typical regional areas or spots associated with all the fiber bundle intersection points.

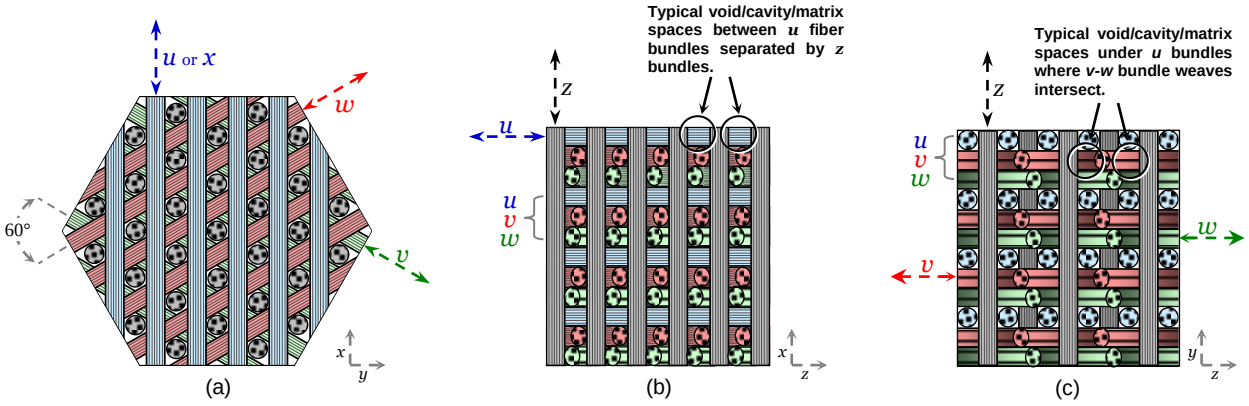

Figure 16. Reproduction of illustrations for the HT-7 preform along the (a) *z*, (b) *u*+90 and (c) *u* orientations indicating typical void regions associated with bundle intersections.

Generally, these spaces will contain deposited C and SiC matrix, but may also include small unfilled volume fractions due to inadequate resin intrusion into the localized region and/or volume closure as a result of too few 3000° heat exposures during the densification process, both of which usually lead to sealed off pores. Completely filled, partially filled or unfilled (void) spaces will occupy all *v*-*w* intersections under *u* layers, all *w*-*u* intersections under *v* layers, and all *u*-*v* intersections under *w* layers as indicated in Figure 16(c). The same can be said of all the local spaces between *u* bundles separated by *z* bundles as well as all the analogous spaces associated with the *v* and *w* bundles, as indicated in 16(b). These latter spaces can be seen in one of the cross-sectional specimens generated by ATK as shown in Figure 17 which gives an image of the perspective represented in 16(b).

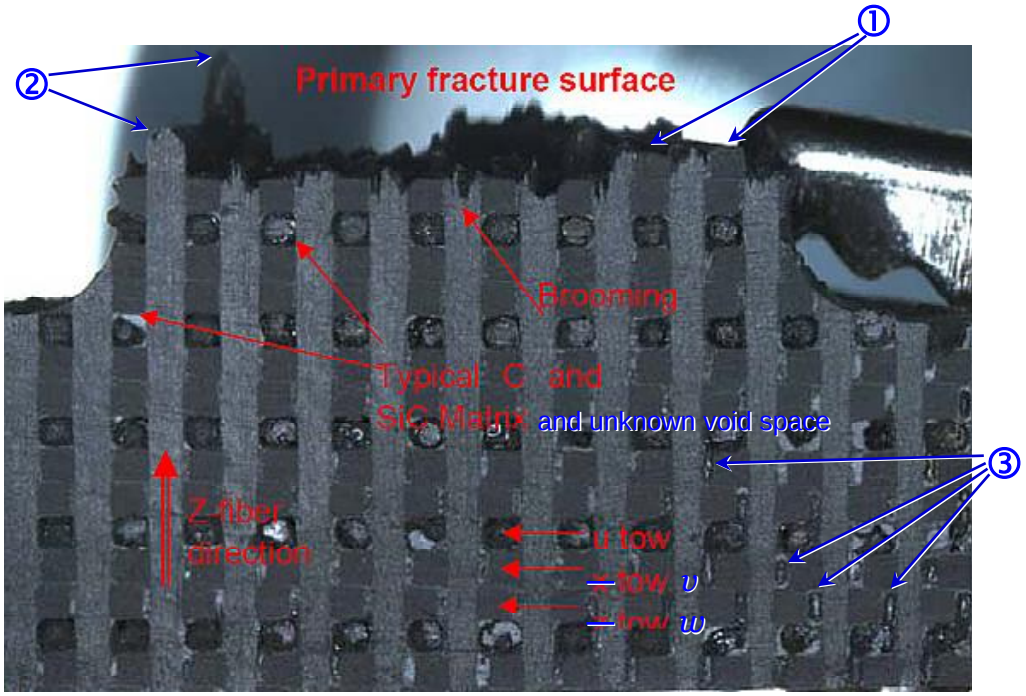

Figure 17. Cross-section of Shaft Side generated during ATK's analysis looking down a *u*+90 direction onto the *x*-*z* plane. ATK notes are given in red, current notes are given in blue.

Here, ATK's analysis is indicated in red while points for the current discussion are given in blue. The specimen has been machined and polished into the *x*-*z* plane to approximately half way through a row of *z* bundles exposing about half of the space separating parallel *u* bundles. As iterated above, it is highly likely that many of these spaces contain porosity or unfilled voids – in addition to the carbon and SiC matrix deposits. Also, as indicated, if this is actually 'brooming' of the failed fiber ends, it would imply that the bundles underwent microbuckling (compression) at some point during the failure process. As ATK has made note of in their report, there are no obvious signs of debonding between the fibers and matrix in this image. This is concurred by observations made earlier in this discussion regarding test data indicating strong fiber-to-matrix bonding (in general, that is . . . again, localized property variations are inherent in this kind of material and are often unpredictable, geographically). A couple of other minor points of interest might be given here . . . ① These are the pair of *v* bundles indicated by ③ in Figure 15. However to correspond visually with the preceding image designations, relative *u*, *v*, *w* designations would have to be re-ordered for this particular view but this is unnecessary since *u*, *v*, *w* designations are arbitrary anyway. ② Possible oxidation or etching may have occurred on these bundle ends as indicated by the softened edges and dulled fiber ends. ③ Matrix/porosity cavities associated with fiber bundle intersections can be seen here and at many other points. They are typically more visible directly along *u*, *v*, *w* orientations as discussed above and indicated in Figure 16(c). It is uncertain whether these are larger than normal since their presence may be more representative of dry preform distortions or deformations. This variability in the weave structure could have been imparted during the weaving process or afterwards during handling/processing of the unrigidized preform.

Disregarding all the valve mechanics and propulsion dynamics for the moment, and focusing only on the material property perspective here, this fracture probably initiated at one of the weak points as indicated earlier. The worst case would consist of machine-damaged *z* bundles near one or more voids and weak interlayer bonding involving short (edge) *u*, *v* or *w* bundles. The failure process likely transpired in stages involving *u*-*v* interlayer separations possibly induced by side loads followed by a buckling-type fatigue (perhaps some kind of tension-compression or flexural cycling) and hot gas exposure until the reinforcing *z* fiber bundles finally broke. Intruding hot gases into the fracture gap region would begin to soften fiber-to-matrix bonds and exacerbate continued *u*-*v* interlayer/interbundle separations (fiber-to-matrix bond failures) allowing the fracture to propagate across the *u*-*v* interface.

It is apparent at this point that closed pores, voids and sealed cavities were opened up during the fracture process, and it should be noted here that these do not necessarily count as part of the measured ~13% porosity reported by XYZ. As mentioned earlier, the Archimedes porosity/density test only quantifies that portion of the porosity, voids and cavities that are accessible to the test fluid, and if the low viscosity / low surface tension SMP-10 resin could not access these pores, chances are the test fluid could not either. Apparently, voids in these regions were inaccessible to the densification process. Most likely, they were sealed off early in the process during the first or second 1500° PIP cycles and not enough 3000° heat treatments were applied across the densification process to effectively open them up for subsquent resin impregnations. It should also be noted that much of the 13% measured porosity is 'microporosity' and cannot be seen with the naked eye (or camera). It can be stated with high confidence that the ~13% porosity reported by XYZ is a combination of . . . (1) microporosity (it is known that micropores, which cannot be seen under low magnification, comprise a substantial fraction of the open porosity[1]), and (2) pores, voids and cavities that were opened up during machining of the test specimens. Thus, it is difficult to substantiate what portion of the total porosity the measured 13% actually represents (undoubtedly, it was the porosity that was available to the intruding test fluid after the test specimen was machined from the billet). The intermediate machining step XYZ used during the manufacturing process not only isolates each of the articles but is also opens up closed pores, similar to what these fractures did. Final machining after the seal coating phase not only removed coating material but may have also opened up pores and cavities that were unavailable through the latter portion of densification process. The primary purpose of the 3000° heat treatments after PIP cycles 5 and 10 is to open up pores by widening existing ones and creating new ones when the bulkier a-SiC converts into the consolidated β-SiC form. This allows resin access into these areas during impregnations, but if there are not enough >2400°-2500° heat exposures during the densification process, permanently sealed voids and closed pores are inevitable.

Details associated with the second failure near the pintle head-to-shaft interface indicate a different failure mechanism than that associated with the first fracture. Only one image was available for this failure and the visual quality is less than ideal. The existence of protruding bundles and porosity/voids is more difficult to make out. See Figure 18

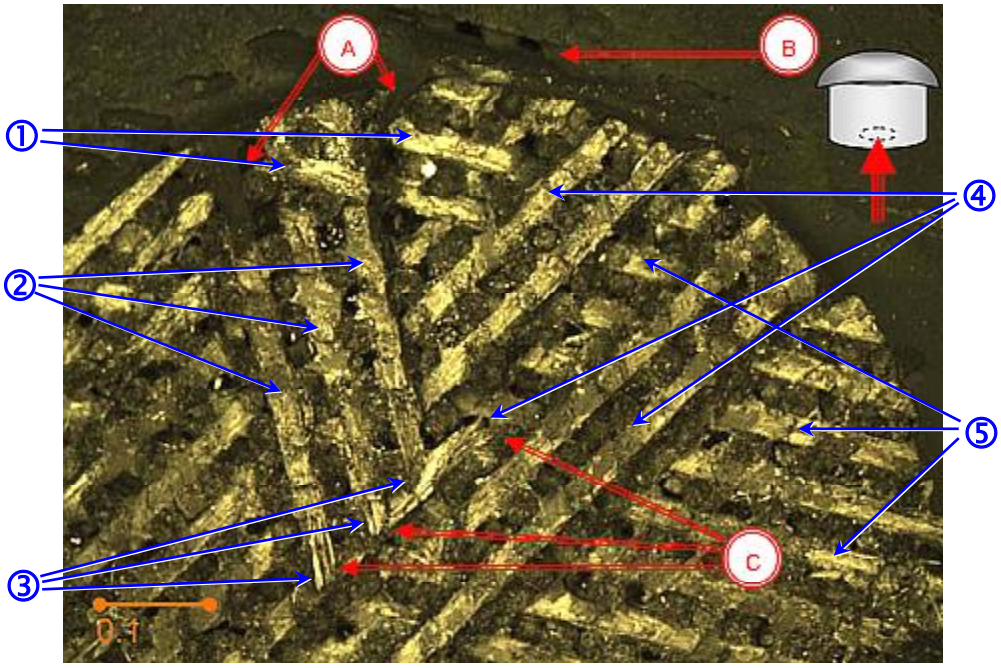

Figure 18. Image of one of the fracture surfaces in the second failure near the shaft-to-head interface.

[1] The existence of microporosity as a significant portion of the total porosity in composite systems has been substantiated by the industry, literature and R&D community as well as direct personal experience in the processing and characterization of these particular material systems.

In this perspective, ATK has provided their notes in red and comments indicated in blue will be given shortly to supplement their notes. Red item "A" included comments associated with the depth of seal coat penetration into the substrate region. The coating material (again, just a modified slurry of SMP-10 polymer resin) was found directly on the fracture surface as indicated by "A". While the machining process incrementally removes material from the surface of the part, it also gives an inside view of the material, exposing pores, voids and cavities that are interconnected deep into the substrate. In addition, weakened interlayer associations between bundle layers, especially the shorter edge bundles, can allow resin penetration directly into the substrate interlayers much deeper than the normal porosity associated with the surface of the article. Either one or both of these effects could have played a role in unusual substrate penetration, but accessibility through separated/delaminated *u-v* layers generated before the motor test (as in the manufacturing or machining processes) could not be ruled out as the primary contributor in the initiation of this fracture. Likewise, a similar condition (weakened interlayer associations near the machined surfaces) could have played a role in the first fracture.

Observation of the fracture surface in Figure 18 reveals that fiber bundles in at least three layers were involved in the fracture. Comments indicated by the blue numbers are given below . . .

① This layer can be designated as the first *u* layer and it can be seen that most of the layer is completely gone (not to be confused with the next *u* layer three layers down which is still intact).

② These three bundle sections appear to be all that is left of the *v* layer. Along part of their length, they were completely torn away as indicated by ③.

④ Much of the *w* layer remains. The middle arrow shows a single *w* bundle that was ripped out and the bottom arrow shows the edge (the last bundle) of the remaining *w* layer.

⑤ This is the second *u* layer down. Other than a few damaged fibers and roughened bundles, this layer remained intact.

These observations lend credence to the general note that this material seems to exhibit strong fiber-to-matrix bonding . . . at least in the body of the article. Near the edges, that is, near the machined surfaces, the conditions associated with composite strength and mechanical properties may not be as impressive as that in the interior of the part. In actuality, machining may do more that just damage *z* bundles but it may also weaken interlayer associations and interbundle bonds near the edges/surfaces of the article resulting in weakened laminar-type interfaces along the contour. Historically, there must be ample evidence in the industry and literature documenting the detrimental effects of machining composite parts. Typically, machined surfaces are designed to be far away from the field/exposure environment or shielded in some fashion, but all the surfaces on the HT-7 articles are freshly machined contours highly dependent on the seal coating process, which is not necessarily 100% continuous. The hand brushed-on coating will inevitably leave some fibers exposed and will cover over many pores rather than fill them, and whenever this material fires, including during the motor test cycle, it undergoes shrinkage, losing volume and increasing in porosity

In this image, there appears to be no indication of thermally weakened fiber-to-matrix bonds as with the first fracture. Also, the lack of combustion deposits along with strong fiber-matrix interactions imply that a cold, one step fracture took place. There is little evidence indicating fatigue effects but rather this fracture could have occurred quickly during the cool down phase of the firing cycle (ATK has made similar comments). It bears a strong resemblance to a 2-D InterLaminar Tensile failure which was pulled off-axis. Pure (ideal) ILT fails along a single interface whereas less-than-ideal ILT failures usually transverse across more than one layer (breaking fiber bundles) due to inadvertent side moments. So it is possible this interface failed due to combined loading in tension and from the side. Damage to the fibers could have been caused by out-of-plane transverse-type shearing forces from a fracture front that started at the top of the image due to interlayer seal coat penetration between *u-v* layers which were weakened, delaminated or separated during the machining process.

Closing Comments

The most significant mechanical detriments to the current XYZ C-C/SiC material and process concept are believed to be associated with (1) The machining process which damages fibers and weakens interlayer (interlaminar) associations, particularly along vulnerable contours or surfaces which can subsequently become fracture initiation points. (2) The unduly low fiber volume fraction of the preform, particularly the lack of true 3-D fiber continuity throughout the *u*, v, w, z structure. In the composites world, fiber volume = mechanical strength. On a macro-scale, the preform bundle structure in this particular 3-D weave may seem to be 'continuous' in a sense, but after machining to the required part dimensions, the bundle (or tow) lengths across the narrow diameter of the HT-7 pintle shaft are quite short, about 0.8" max, and the edge bundle lengths are even shorter. More importantly, there is absolutely no continuity or weave interlacing between adjacent *u*, *v*, *w* layers or bundles in any direction. The presence or lack of these interaction features has a profound effect on the composite's mechanical behavior and the effectiveness of the fiber volume fraction. In actuality, the *u*, *v*, *w* bundles in this configuration are not much different than oriented chopped fibers. (3) Too high of a level of closed porosity, sealed voids and impermeable cavities. While the total porosity picture in almost any fiber/matrix composite system will inevitably include a certain level that is inaccessible, reduction or elimination (if it were possible), of the impenetrable porosity fraction should be of prime importance. By analogy, it could also be said that high levels of closed porosity = poor mechanical strength.

There are no declarations given here proposing that any of these conditions can necessarily be solved or significantly improved with current state-of-the-art capabilities or without incurring enormous expenses in the process. These are merely stated for the record and to raise awareness of some of the likely issues that seem to be limiting this material concept from its potential capabilities. As such, freedom will exercised here to make comments and recommendations regardless of their exact correctness or how impractical they may seem to some.

By design, the pintle article is intended to obtain most of its mechanical strength from the *z* fiber bundles. However, if the perpendicular interlayer planes at the surface of the part are weakened during the machining process, the *z* bundles cannot perform their function effectively and the impinging interlayer fracture front will dominate the mechanical behavior of the article. If weak interlayer interactions are coupled with *z* bundles also damaged from the machining process, the situation is exacerbated since the *z*-oriented fiber volume is reduced and the partially machined bundles are rendered essentially ineffective. Needless to say, circumferential machining of the narrow shaft resulting in a groove or localized recession, automatically becomes the weakest link in the entire structure.

The most viable alternative to machined articles is the use of continuously woven preform structures that are woven at or very near net shape and dimensions. This technology is currently available to varying degrees through companies such as Intermat (XYZ), 3TEX and EDO (ITT). The cost may or may not be prohibitive . . . no inquiries have been made at this point. These companies are also the ones to talk to about increasing fiber volume levels in their preform weaves. Bear in mind however, it may not be practical to increase weaving density too much without imparting significant damage to the reinforcing fibers. In lieu of this, specialized compaction methods coupled with the weaving process should be explored. If it were physically feasible and cost effective, higher fiber volume 3-D weaves or braids woven to near net dimensions would solve most of the reinforcement problems at issue and allow the team to focus more on motor/valve design rather than material problems. Very short chopped fibers or nanotubes, if incorporated properly (perhaps during the rigidization process), could increase the total fiber volume fraction (and the toughness) of the composite and this would have a moderate effect on strength improvement but would add nothing to the requirement for increased levels of continuous reinforcement. If these components flocculated, specific patterns could enhance composite mechanicals, but if they agglomerate, this approach would likely clog up more pore channels and increase the levels of closed porosity, which is another condition that needs to addressed with the current design.

For most polymer matrix composites, the resultant tensile strength theoretically should be . . . $E_R = f_v E_T \sim 95\,ksi$ where $f_v \simeq 14\%$ and $E_T = 670\,ksi$ corresponding to the effective *z* fiber volume and bundle tensile strength for the current HS40-based material under investigation. This represents about 20% transfer efficiency of the fiber strength to the composite level, which is quite poor. It is well out-of-line with the measured levels given in Table 1 mainly because the highly brittle nature of the C/SiC matrix degrades the assumptions of elasticity that the rule of mixtures is based upon. But it is suspected that other factors also play a role in the ineffective transfer of fiber strength to composite strength that are inherent to this particular preform or composite design. For most of the *u*, *v*, *w* properties, this particular composite system is matrix-dominated. Due to the low overall fiber volume, matrix properties also dominate some of the *z* attributes. In general, traditional fiber-dominated properties will be heavily influenced by matrix contributions in any direction.

It is firmly believed that these slabs did not see enough high temperature exposures during the densification process (2400°-2500° is the proposed minimum temperature range needed to open up the porosity during the conversion $\alpha\text{-}SiC \rightarrow \beta\text{-}SiC$). Most likely, unfilled voids and cavities at bundle intersections are permanently sealed off during one of the first three PIP cycles and then the single 3000° heat treat step following the 5th PIP cycle is ineffective at opening up all the available pore spaces. There is ample historical evidence as well as direct experiences demonstrating that impregnating too much matrix precursor on top of itself before subjecting the article to full pyrolytic conversion leads to closed pores and voids which ultimately lead to inferior products (plagued with weak planes, delaminations and premature fractures due to internal pore pressures). In addition, lack of the application of external pressure during each of the PIP cycles decreases the potential effectiveness of the resin densification process (as with the overwhelming majority of CMC fabricators, XYZ probably only uses vacuum during their SiC PIP cycles). Application of the 1550° pyrolysis followed by a separate 3000° heat treat step at cycle 5 is not necessary (and it takes more time), . . . rather a single 3000° pyrolysis would be quite satisfactory. But again, and most importantly, two 3000° exposures are simply inadequate to properly densify this material (currently, one heat treat is applied after the 5th and 10th cycles). It would be strongly recommended here that the substrate be subjected to 3000° pyrolysis after each impregnation/cure, rather than the current 1550°, in order to improve porosity infiltration throughout the billet, reducing the level of closed pores and potentially reduce the total process time. Ideally, each PIP cycle should consist of vacuum/pressure resin impregnation followed by 3000° pyrolysis. Reducing any of these factors reduces the quality of the part.

Also, some companies disperse fine SiC particles in the impregnating resin to create particulate slurries for densifying the substrates (rather than just using neat resin). The intent is to reduce the number of densification cycles needed to bring the substrate up to the required density (and strength) levels. It is unknown if FMI employs this approach. However, no matter how you perform it, this practice is known to clog up pore openings and channels. It is difficult enough just to get the neat resin into the deepest pores. By closing off and blocking pore entrances during the impregnation process, the use of particulate-filled densification resins gives the false impression that fewer cycles are needed, but in the end it produces inferior parts with higher levels of closed pores.

Supposedly, the inner-most regions of the composite porosity contain SiC matrix fractions that are made up of crystalline β-SiC, while increasing levels of glassy a-SiC become prevalent in the outer matrix regions, and close to 100% a-SiC comprises the outer layers of the matrix/coating phase near the surface of the article. For informational purposes, it might be interesting to review and contrast a few of the differences between these two polymorphs.

> Glassy (amorphous) a-SiC will begin to undergo conversion (crystallization) into β-SiC when exposed to temperatures above about 2000°. If this conversion takes place in the motor/valve environment, the converted matrix assumes the properties of β-SiC. Conversion volume reductions and CTE differences between the two phases may result in microcrack formation.

> Notable bulk volume reductions and porosity creation accompany the conversion of a-SiC into β-SiC. These may take the form of surface craters, cavities and irregularities, possibly exposing the substrate surfaces underneath. In addition, these volume reductions may result in microcracks.

> Due to its amorphous structure, a-SiC appears to exhibit a lower CTE, lower conductivity and higher shock protection than β-SiC Also, glassy a-SiC has a lower density than its condensed β-SiC counterpart (2.4 to 2.5 vs. 3.0 to 3.1).

> The crystalline β-SiC phase is more prone to microcracking. The absence of microcracking in the glassy a-SiC fraction suggests that this amorphous phase has a lower CTE and/or a lower elastic modulus.

> During slow mechanical loading processes, crystalline β-SiC is more effective at transferring the load to the fibrous reinforcement and is better for applications requiring high heat conduction through the part. Heat conduction through β-SiC is even higher than that through the carbonized pitch matrix.

> The glassy 'green' form a-SiC is more susceptible to oxidative degradation. While there is a discernable boundary between β-SiC and its amorphous SiO_2 passivation (oxide) layer, the amorphous structure of a-SiC tends to dissolve its oxide layer which probably becomes a mixture of SiC-SiO_2.

Preforms woven from pitch-coated fiber tow would improve interbundle and intrabundle porosity infiltration and perhaps provide an innovative way to rigidize the preform with minimal distortions and deformations. These benefits would be established within the preform structure before the primary densification process begin thus reducing many opportunities for pore closure.

Impregnations using green pitch and/or stage A monomers/oligomers would improve (a) matrix infiltration within the inner-most porosity channels; (b) fiber-to-matrix intimacy and bonding; and (c) fiber surface wetting and penetration. Pitch carbon precursors and SMP-10 can both be tailored as materials of low molecular weight and low degree of polymerization.

Recent XYZ C-C/SiC articles have been fabricated using the former AlliedSignal's 15V coal tar pitch as the carbon matrix precursor. However, Allied was acquired by Honeywell a few years back and now there is word that XYZ may be switching to Marathon's petroleum-based pitch M50. Petroleum pitches contain more aliphatic carbons and fewer aromatic rings (benzene rings are the ideal precursor for high carbon yield). Depending on the grade and coking value, more densification cycles may be needed using petroleum-based pitches in order to achieve the same char yield as that with coal tar pitches.

As with the amorphous vs. crystalline structure of SiC, amorphous carbon forms exhibit notable differences compared to graphitized carbons. By analogy, these comparisons are similar. That is, graphite is a strong conductor with higher density, and better transfer of thermal/mechanical loads to the reinforcement during slow loading while amorphous carbons exhibit lower densities, absorb heat and mechanical waves providing better shock protection to the composite fibers.

SiC fibers derived from SMP-10 polymer and other precursors are now available as an alternative to carbon fiber reinforcements in extremely high temperature oxidative applications such as engine components. These SiC/SiC composites exhibit higher modulus than their carbon fiber counterparts but comparable strength levels. Some of the most notable benefits include high temperature oxidation resistance and strength retention at high temperatures. Low oxygen versions of Sylramic, Tyranno and Nicalon brand SiC fibers are commercially available and being used for composites derived from woven 3-D preforms, needled and z-stitched configurations. Needless to say, they provide excellent thermal, mechanical and interface compatibility with SiC matrices.

Appendix

Many of the initial expressions given here can now be found in common literature sources, however, most of the subject matter dealing with C-C/CMC densification processing is not as easy to find. The following is based on concepts developed during an extensive series of densification studies conducted throughout the period 1982 -1990 and originally issued in the report, “Relationships In Carbon-Carbon Substrate Processing”, Randy Lee, LTV Aerospace & Defense Co., Space Shuttle LESS Program, 1985. The version that follows has been adapted and re-formatted specifically to address the current discussion at hand regarding FMI’s CMC material processing. Since this modified version was 're-created' rather quickly, errors cannot be ruled out.

At any point during the fabrication (or lifetime) of a composite substrate, the bulk density can be defined as the sum of the products of each constituent density and its respective volume fraction . . .

$$\rho_b = \frac{w_f + w_m}{V} = \frac{\rho_f v_f + \rho_m v_m}{V} = f_v \rho_f + m_v \rho_m$$

where w_f, w_m, v_f and v_m are the actual weights and volumes of the fiber and matrix phases comprising the slab, billet or article which has an actual weight and volume of W and V. Accordingly, ρ_f and ρ_m are the impervious fiber and matrix densities, and f_w, m_w, f_v, m_v and p are the fiber and matrix weight fractions, along with the fiber, matrix and porosity volume fractions respectively.

Here, it is realized that the total weight of a slab or panel is always equal to the sum of weights of all of its constituents while the total volume is always equal to the sum of volumes of all the constituents . . .

$$W = w_f + w_m \qquad \text{and} \qquad V = v_f + v_m + p$$

In these types of composites, both the physical weight and volume of the fiber are usually considered to be constant throughout the process while, the total matrix weight may itself be a sum of several components such as carbon, ceramic and/or resin . . . $w_m = w_c + w_{SiC} + w_r$

Also, the sum of fractions by weight and the sum of fractions by volume are always unity. Respectively . . .

$$f_w + m_w = 1 \qquad \text{and} \qquad f_v + m_v + p = 1$$

Fiber and matrix volume fractions can be expressed in terms of their respective weight fractions. Since . . .

$$\rho_f = \frac{w_f}{v_f} = \frac{f_w W}{f_v V} = \frac{f_w}{f_v}\rho_b \qquad \text{then . . .} \qquad f_v = f_w \frac{\rho_b}{\rho_f} = (1 - m_w)\frac{\rho_b}{\rho_f}$$

$$\text{Likewise . . .} \qquad m_v = m_w \frac{\rho_b}{\rho_m}$$

The true or real composite density (sometimes called the skeletal or impervious density) refers to the non-porous portion of the substrate (i.e... the fiber and matrix only). While the bulk density is defined by constituent volume fractions, the true composite density is a function of the weight fractions and approaches the bulk density when the pore volume approaches zero . . .

$$\rho_t = \frac{W}{v_f + v_m} = \frac{W}{V - v_p}$$

$$\rho_t = \rho_b \left(1 - p\right)^{-1}$$

With inclusion of the porosity fraction, the bulk density can be written in terms of component weight fractions. . .

(1A) $$\rho_b = \frac{W}{v_f + v_m + v_p} = \left(f_w \rho_f^{-1} + m_w \rho_{\mathrm{m}}^{-1} \right)^{-1} \left(1 - p\right)$$

Rearrangement of Eq(1A) gives an expression for estimating the porosity from the fiber density, matrix density and matrix content. This formula has come in very handy for numerous material systems over the years . . .

(2A) $$p = 1 - \rho_b \left[\left(1 - m_w\right) \rho_f^{-1} + m_w \rho_m^{-1} \right]$$

Now at the beginning of the densification process, the rigidized preform structure is pitch impregnated and then subjected to pyrolysis which converts the pitch material into a non-melting, pre-graphitc mesophase carbon. As ceramic densification commences, the slab undergoes sequential cycles of SMP-10 pre-ceramic polymer resin impregnation/cure followed by pyrolysis to convert the cured polymer into SiC ceramic (the slab is weighed before and after each step). The CMC densification process is defined essentially by three parameters: (1) the positive weight gain η_g that occurs when an article in a pyrolyzed state (i) is impregnated with polymer/resin to a bimatrix state (iB), and (2) the positive weight loss η_l that occurs due to pyrolysis of the article in a bimatrix (impregnated) state (iB) to the next corresponding ceramic state ($i+1$). These two parameters result in changes exclusively within the matrix and are represented respectfully by . . .

$$\eta_{g,i} = \frac{W_{iB} - W_i}{W_i} = \Delta m_{w,i \to iB} \qquad \text{and} \qquad \eta_{l,i+1} = \frac{W_{iB} - W_{i+1}}{W_{iB}} = \Delta m_{w,iB \to i+1}$$

bimatrix weight gain at state *i* to state *iB* — pyrolysis weight loss at state *iB* to state *i*+1

Each step in the process can be recognized by subscripts denoting the preform state $i = P$, the single carbon (C-C) state $i = 0$, any one of the subsequent ceramic (pyrolyzed) states, $i = 1, 2, 3, \ldots$, or one of the intermediate impregnated (bimatrix) states, $iB = 0B, 1B, 2B, \ldots$ At any given state in the process, the matrix will consist of one or more of the following: (1) a fixed level of inorganic pre-graphitic carbon (established during the initial pitch densification step); (2) previously deposited inorganic SiC ceramic (whose fraction cumulatively increases over the matrix densification process); and (3) unconverted pre-ceramic, semi-organic SMP polymer which has just been impregnated into the porosity of the composite. For the convenience of this discussion, the term 'bimatrix' will simply refer to one of the impregnated states prior to pyrolysis.

(3) The cumulative ceramic weight gain η_{SiC} from the initial ceramic (pyrolyzed) state to any future ceramic (pyrolyzed) state is the total converted ceramic matrix material deposited within the pores of the composite and represents the change in matrix content as the article progresses from the state $i = 0$ to the state i . . .

$$\eta_{SiC,0\rightarrow i} \;=\; \frac{W_i - W_0}{W_0} \;=\; \Delta m_{w,0\rightarrow i}$$

While the state $i = 0$ is actually the substrate's only carbon state, for convenience, the nomenclature used here may often refer to it as the first ceramic state. Note that only pyrolyzed states are involved in this estimate (no bimatrix states). Thus, $\eta_{SiC,0\rightarrow i}$ is the net effect of all the impregnations/pyrolysis densification cycles.

Now at the state $i = P$ there is no matrix fraction (neglecting the rigidization coating for the moment) and the billet consists only of the dry woven preform structure whose weight is the same as the fiber weight $W_P = w_f$, which remains constant throughout. Estimates involving weight changes that occur during matrix densification typically pertain to varying matrix constituents while constant quantities tend to cancel out. Components such as the fiber weight and volume w_f and v_f do not play a role in the matrix densification process and are eliminated in the calculations, while those pertaining to the initial carbonized pitch fraction such as w_c and v_c are only relevant during the initial C-C stage and vanish beyond that . For instance, the weight gained by the dry preform billet as a result of the pitch impregnation and pyrolysis/carbonization cycle during conversion from the step $i = P$ to the first ceramic (or carbon) state at $i = 0$ is given by . . .

$$\eta_{g,P} = \frac{W_0 - W_P}{W_P} \;=\; \frac{w_c}{W_P} \;=\; \frac{w_c}{w_f}$$

where the preform substrate weight changes by $W_P = W_0\left(1+\eta_{g,P}\right)^{-1}$ and the total matrix weight fraction at $i = 0$ becomes $m_{w,0} = w_c / W_0$ . . . or . . .

(3A) $$m_{w,0} = 1 - \frac{w_f}{W_0} \;=\; 1 - \frac{w_f}{W_P\left(1+\eta_{g,P}\right)} \;=\; 1 - \left(1+\eta_{g,P}\right)^{-1}$$

At the first pyrolyzed state, the matrix consists solely of inorganic carbon deposit, so the total matrix weight and associated weight fraction (total matrix content) is just that of the carbon, respectfully . . . $w_{m,0} = w_{c,0}$ and $m_{w,0} = m_{c,0}$ (the rigidization material probably comprises less than 1% of the matrix and will be neglected here). The pitch impregnation/pyrolysis step starts the matrix densification process by coating about 17 to 19% carbonized pitch onto the pore walls and fiber surfaces of the undensified preform. But there is still much porosity to be filled with subsequent SiC densification cycles, which comprise the overwhelming majority of the densification process. The first impregnation/cure with SMP-10 polymer takes the substrate from the ceramic state $i = 0$ to the bimatrix state $i = 0B$ in which the total weight of matrix is $w_{m,0B} = w_c + w_{SiC',0}$ and the total matrix content becomes $m_{w,0B} = m_{c,0} + m_{SiC',0B}$ (where SiC' refers to cured but unconverted semi-organic SMP-10 polymer and SiC is just SiC ceramic).

The polymer impregnation (or infiltration) step is carried out on the article in a vacuum chamber in which vacuum pressure is used to force liquid SMP-10 polymer resin into the pores of the substrate. After manually removing excess resin from the surfaces of the slab, it is cured in an autoclave to crosslink and harden the polymer in place. The impregnation/cure weight gain that occurs as the substrate is taken from the $i=0$ ceramic state to the $i=0B$ bimatrix state is . . .

$$\eta_{g,0} = \frac{W_{0B} - W_0}{W_0} = \frac{w_{SiC',0B}}{W_0}$$

In this step, the substrate weight is changed by the amount $W_0 = W_{0B}\left(1+\eta_{g,0}\right)^{-1}$ while the original preform billet changes by $W_P = W_{0B}\left(1+\eta_{g,0}\right)^{-1}\left(1+\eta_{g,P}\right)^{-1}$. The matrix content at the bimatrix state $i=0B$ is then . . .

$$m_{w,0B} = 1-\frac{w_f}{W_{0B}} = 1-\frac{w_f}{W_0\left(1+\eta_{g,0}\right)}$$

$$m_{w,0B} = m_{w,0}\left(1+\eta_{g,0}\right)^{-1}$$

or in terms of the original pitch densification weight gain . . .

$$m_{w,0B} = 1-\left(1+\eta_{g,P}\right)^{-1}\left(1+\eta_{g,0}\right)^{-1}$$

After the $0B$ impregnation and cure, the substrate is subjected to low temperature pyrolysis which converts the crosslinked polymer matrix into amorphous silicon carbide (a-SiC). The ceramic yield y is the weight of cured pre-ceramic polymer remaining after pyrolysis, that is, $y = SiC'/SiC$, a constant which runs in the 75-85% range for SMP-10 (precise measurements of y are typically acquired by the manufacturer and/or vendor). Thus, the pyrolysis weight loss that occurs as the substrate is converted from the $0B$ bimatrix state to the second ceramic state $i=1$ is . . .

$$\eta_{l,1} = \frac{W_{0B} - W_1}{W_{0B}} = \frac{W_{SiC',0B}\left(1-y\right)}{W_0\left(1+\eta_{g,0}\right)_0}$$

which becomes . . . $\eta_{l,1} = \eta_{g,0}\left(1-y\right)\left(1+\eta_{g,0}\right)^{-1}$

Here, the substrate weight changes by . . . $W_{0B} = W_1\left(1-\eta_{l,1}\right)^{-1}$ while the original preform weight is modified accordingly . . . $W_P = W_1\left(1-\eta_{l,1}\right)^{-1}\left(1+\eta_{g,0}\right)^{-1}\left(1+\eta_{g,P}\right)^{-1}$, and the total matrix content then becomes . . .

$$m_{w,1} = 1-\frac{w_f}{W_0\left(1+\eta_{g,0}\right)\left(1-\eta_{l,1}\right)}$$

$$m_{w,1} = 1-\left(1+\eta_{g,P}\right)^{-1}\left(1+\eta_{g,0}\right)^{-1}\left(1-\eta_{l,1}\right)^{-1}$$

Thus, the matrix content at each of the ceramic states can be given by . . .

at $i = 0$ . . . $\quad m_{w,0} = 1 - \left(1 + \eta_{g,P}\right)^{-1}$

at $i = 1$ . . . $\quad m_{w,1} = 1 - \left(1 + \eta_{g,P}\right)^{-1}\left(1 + \eta_{g,0}\right)^{-1}\left(1 - \eta_{l,1}\right)^{-1}$

at $i = 2$ . . . $\quad m_{w,2} = 1 - \left(1 + \eta_{g,P}\right)^{-1}\left(1 + \eta_{g,0}\right)^{-1}\left(1 - \eta_{l,1}\right)^{-1}\left(1 + \eta_{g,1}\right)^{-1}\left(1 - \eta_{l,2}\right)^{-1}$

. . . and so on . . .

In general . . .

(4A) $$m_{w,i} = 1 - \left(1 + \eta_{g,P}\right)^{-1} \prod_{0}^{i} \left(1 + \eta_{g,i-1}\right)^{-1}\left(1 - \eta_{l,i}\right)^{-1}$$

which allows estimation of the total matrix weight fraction at any subsequent process state based on the original carbonized pitch weight gain in the preform billet.

All this is simply an extension of what happens to the initial dry preform weight W_P as it incrementally and sequentially progresses through the densification process to the state i . . .

$$W_P = W_0\left(1 + \eta_{g,P}\right)^{-1} = W_1\left(1 + \eta_{g,P}\right)^{-1}\left(1 + \eta_{g,0}\right)^{-1}\left(1 - \eta_{l,1}\right)^{-1} = W_i\left(1 + \eta_{g,P}\right)^{-1} \prod_{0}^{i} \left(1 + \eta_{g,i-1}\right)^{-1}\left(1 - \eta_{l,i}\right)^{-1}$$

The cumulative ceramic weight gain from the first pyrolyzed state ($i = 0$) to any future ceramic (pyrolyzed) state is a function only of the SiC ceramic gain (rather than the total matrix), accordingly . . .

$$\eta_{c,0\to i} = m_{SiC,i} \prod_{1}^{i} \left(1 + \eta_{g,i-1}\right)^{-1}\left(1 - \eta_{l,i}\right)^{-1}$$

A plot of $\eta_{c,0\to i}$ should parallel that of the matrix content as it progresses through the process.

Now the matrix content can be expressed in terms of the progressive state densities by recognizing that the bulk volume of the preform/substrate remains constant throughout the process (state-to-state bulk volume changes, if they occur, are infinitesimal) . . .

$$\eta_{g,(i-1)} = \frac{W_{(i-1)B} - W_{(i-1)}}{W_{(i-1)}} = \frac{\rho_{b,(i-1)B} - \rho_{b,(i-1)}}{\rho_{b,(i-1)}} \qquad \text{and} \qquad \eta_{l,i} = \frac{W_{(i-1)B} - W_i}{W_{(i-1)B}} = \frac{\rho_{b,(i-1)B} - \rho_{b,i}}{\rho_{b,(i-1)B}}$$

which means that . . $\left(1 + \eta_{g,(i-1)}\right) = \rho_{b,(i-1)B} / \rho_{b,(i-1)}$ and $\left(1 - \eta_{l,i}\right) = \rho_{b,i} / \rho_{b,(i-1)B}$

and finally (for ceramic states only) . . .

(5A) $$m_{w,i} = 1 - \prod_{P}^{i} \rho_{b,i-1} / \rho_{b,i}$$